Editors' Suggestion

Cost and routing of continuous-variable quantum networks

Federico Centrone [1,2,*] Frederic Grosshans,[1,†] and Valentina Parigi [3,‡]
[1]*Sorbonne Université, CNRS, LIP6, 4 place Jussieu, F-75005 Paris, France*
[2]*Université de Paris, CNRS, IRIF, 8 Place Aurélie Nemours, 75013 Paris, France*
[3]*Laboratoire Kastler Brossel, Sorbonne Université, CNRS, ENS-Université PSL, Collège de France, 4 place Jussieu, F-75252 Paris, France*

(Received 29 June 2023; accepted 29 September 2023; published 20 October 2023)

We study continuous-variable graph states with regular and complex network shapes, and we report their cost as a global measure of squeezing and the number of squeezed modes that are necessary to build the network. We provide an analytical formula to compute the experimental resources required to implement the graph states, and we use it to show that the scaling of the squeezing cost with the size of the network strictly depends on its topology. We show that homodyne measurements along parallel paths between two nodes allow one to increase the final entanglement in these nodes, and we use this effect to boost the efficiency of an entanglement routing protocol. The devised routing protocol is particularly efficient in running time for complex sparse networks.

DOI: 10.1103/PhysRevA.108.042615

I. INTRODUCTION

Network science has been used to model the structures and properties of many biological, physical, and technological systems, including the internet and the World Wide Web. Photonics quantum networks are essential resources for quantum information processing and notably for quantum internet applications, where quantum states of light will allow for the efficient distribution and manipulation of information [1–4]. To develop large-scale quantum communications and build a quantum internet it is compulsory to grasp the potentialities of quantum networks and exploit all their exceptional features. We can expect that complex network theory can be used, like in the case of classical networks, to study and drive efficient quantum complex network design for quantum technologies [5].

In this work we study continuous variable (CV) quantum networks in the form of CV graph states with regular and complex topologies. CV quantum information describes quantum states living in infinite dimensional Hilbert spaces; protocols mainly rely on coherent (homodyne) detection which, differently from photon counting detectors, can be highly efficient at room temperature. Moreover, CV quantum networks can be generated deterministically with a large number of nodes [6–10], they can be easily reconfigured [11–14], and they have been also exploited in quantum advantage demonstrations [14].

It is known that the quantum feature of CV states can be lost because of losses and noise during transmission. Nevertheless, substantial progress has been made in CV quantum state distribution [15] and CV quantum repeater design [16]. Moreover, CV quantum networks, which are easily reconfigurable and with a large number of components [7,8,10,14], can be easily exploited as local area quantum networks.

In this work we discuss Gaussian graph states using mathematical tools from network science to estimate how the cost of their experimental implementation is affected by the topology and the size of the network. In particular, we derive an equation providing the squeezing values required to experimentally build a graph state as a function of its graph spectrum. We then adopt a resource theory of squeezing to estimate the cost of expanding the network. Although in entangled qubits networks the resource usage is always proportional to the number of links, we show that in CV Gaussian networks the trend of the squeezing cost presents nontrivial scaling with the size of the network and this is strictly dependent on its topology.

Thereafter, we propose a CV architecture for the quantum internet based on the Gaussian network previously described. We simulate quantum communication protocols through the network by letting the spatially separated agents present at each node perform a homodyne measurement on their optical mode and look for the optimal measurement strategy to maximize the logarithmic negativity—an entanglement measure [17–19]—of the entangled pair shared by the two users who want to communicate, Alice and Bob. We prove that when multiple entangled paths connect Alice to Bob the optimal measurement strategy allows one to increase the logarithmic negativity in the final pair. This *parallel enhancement of entanglement* can be used to increase the quality of quantum communications in some selected network topologies.

Last, we employ our previous findings to implement a heuristic routing protocol for distributing and boosting the entanglement between two arbitrary agents. The algorithm we provide, on the one hand, is much more efficient than directly checking all possible combinations of quadrature

*Also at ICFO-Institut de Ciencies Fotoniques, Castelldefels (Barcelona), Spain; federico.centrone@icfo.eu
†frederic.grosshans@lip6.fr
‡valentina.parigi@lkb.upmc.fr

measurements, and, on the other hand, it always provides higher logarithmic negativity than the classical scheme, which directly employs the shortest path between Alice and Bob and neglects the parallel channels.

II. GAUSSIAN QUANTUM NETWORK

A. Gaussian quantum states

The generation of continuous variables multimode entangled states has been demonstrated in several optical setups. In such experiments we recover network structures as naturally appearing entanglement correlations [20], reconfigurable Gaussian interactions [11], or imprinted cluster states [7–10,21].

These quantum states produced via parametric processes and linear optical transformations are characterized by Gaussian statistical distribution of the quadratures of the involved optical modes [22]. The quadratures $\hat{q}_j$ and $\hat{p}_j$ of the jth mode are canonical conjugate variables, such that $[\hat{q}_j, \hat{p}_k] = i\delta_{j,k}$, associated with the quantum harmonic oscillator describing the light mode. In this work we adopt the following relation with creation and annihilation operators $\hat{\mathbf{a}}^\dagger = (\hat{\mathbf{q}} - i\hat{\mathbf{p}})/\sqrt{2}$ and $\hat{\mathbf{a}} = (\hat{\mathbf{q}} + i\hat{\mathbf{p}})/\sqrt{2}$, such that the variance of the vacuum quadratures is normalized to $1/2$.

The produced states can then be completely characterized by the first two moments of the quadratures $\bar{\mathbf{r}} = \mathrm{Tr}[\rho\hat{\mathbf{r}}]$ and $\sigma = \mathrm{Tr}[\rho\{(\hat{\mathbf{r}} - \bar{\mathbf{r}}), (\hat{\mathbf{r}} - \bar{\mathbf{r}})^T\}]$, where ρ is the density matrix of the Gaussian state and $\hat{\mathbf{r}} = (\hat{q}_1 \dots \hat{q}_N, \hat{p}_1 \dots \hat{p}_N)$; we follow here qp ordering.

Parametric processes are described by quadratic Hamiltonians $\hat{\mathcal{H}}_I = \hat{\mathbf{r}} H \hat{\mathbf{r}}^T$, whose dynamics is implemented on the quadratures by $S_H = e^{\Omega H t}$, as

$$\hat{\mathbf{r}}' = S_H \hat{\mathbf{r}}_0, \tag{1}$$

where $\hat{\mathbf{r}}_0$ are quadratures of the initial state, $\hat{\mathbf{r}}'$ are the quadratures of the final state, and $\Omega = \left(\begin{smallmatrix} 0 & \mathbb{1} \\ -\mathbb{1} & 0 \end{smallmatrix}\right)$ is a $2N \times 2N$ skew-symmetric matrix associated with the N-dimensional Hilbert space allowing us to write the commutation relation of the canonical variables as

$$[\hat{\mathbf{r}}, \hat{\mathbf{r}}^T] = i\Omega = i\begin{pmatrix} 0 & \mathbb{1} \\ -\mathbb{1} & 0 \end{pmatrix}.$$

Since any pure Gaussian state can be obtained by the application of a unitary generated by a quadratic Hamiltonian H to the vacuum, the most general pure Gaussian state covariance matrix is given by applying S_H by congruence to the vacuum covariance matrix $\sigma_0 = \mathbb{1}/2$:

$$\sigma = S_H \sigma_0 S_H^T = \frac{S_H S_H^T}{2}. \tag{2}$$

Singular value decomposition allows one to write the symplectic transformation in the so-called Bloch-Messiah decomposition [22] as a product of an orthogonal, a diagonal, and an orthogonal matrix $S_H = O\Delta O'$, which can be interpreted as a basis rotation, a squeezing in the diagonal basis, and another rotation. The mode basis in which the covariance matrix is diagonal and each component is independently squeezed is named the supermode basis. In [7,20] where the pump and the phase matching function can be described by a Gaussian spectral profile, the supermode basis corresponds to Hermite-Gauss spectral modes. The squeezing values of Δ can be derived from the eigenvalues of the Hamiltonian $\hat{\mathcal{H}}_I$, while the orthogonal matrix O can be interpreted as a measurement basis change or, equivalently, as a passive linear optical transformation. The other orthogonal matrix O' is simplified in the product $S_H S_H^T$ and can be disregarded:

$$\sigma = \frac{S_H S_H^T}{2} = \frac{1}{2} O \Delta^2 O^T. \tag{3}$$

The diagonal matrix Δ contains the information on the minimum number of squeezed modes in the system and their value of squeezing, which will later be used in the chosen resource theory. If we consider a single-mode field, the squeezing operation is defined as a Gaussian transformation that reduces the variance of $\hat{p}$ by a factor $10^{-s/10}$, where s, measured in dB throughout this article, is called the *squeezing factor*. Squeezing is represented by the local symplectic matrix

$$S_{sq}(s) = \begin{pmatrix} 10^{s/20} & 0 \\ 0 & 10^{-s/20} \end{pmatrix}.$$

The multimode Δ matrix can then be written as

$$\Delta = \mathrm{diag}\big\{10^{s_1/20}, 10^{s_2/20}, \dots, 10^{s_N/20}, 10^{-s_1/20}, 10^{-s_2/20}, \dots, 10^{-s_N/20}\big\}. \tag{4}$$

This formalism can be used to visualize and manipulate Gaussian quantum states, which are readily available in most well-equipped photonics laboratories, and, although the number of modes and their connections is still in large part limited, many efforts are employed to improve the capacities of these systems.

Targeted Gaussian quantum states, including the quantum networks of the next section, can be generated via the two following strategies: (1) by tailoring Hamiltonians $\hat{\mathcal{H}}_I$ of multimode parametric processes in order to get the decomposition of Eq. (3) corresponding to the desired covariance matrix [6,7,23–26]; and (2) by getting a number of single-mode squeezers equal to the number of elements with $s_j \neq 0$ of Δ in Eq. (3) and producing the corresponding s_j squeezed states, which are injected in a linear optic intereferometer corresponding to the orthogonal matrix O in Eq. (3) [27–29].

B. Graph states as quantum networks

The above formalism can be employed to describe Gaussian graph states that can be used as CV quantum networks. We at first recall that a network is mathematically described by a graph $\mathcal{G}(V, E)$, which is a set of vertices V (or nodes) connected by a set of edges E. Labeling the nodes of the graph in some arbitrary order, we can define a symmetric adjacency matrix $A = A^T$ whose (j, k)th entry A_{jk} is equal to the weight of the edge linking node j to node k (with no edge corresponding to a weight of 0). Typically, the adjacency matrix is enough to completely characterize a graph; however, we will see that in our case there are other degrees of freedom such as the squeezing of a node and its angle.

We can now describe the quantum networks we use in this work, which are called graph- or cluster states [30–32].[1] Theoretically, they can be built by entangling several squeezed modes of light via CZ gates, which is a Gaussian operation implementing a correlation of strength g between the $\hat{q}$ and the $\hat{p}$ of the two modes on which it acts. The corresponding symplectic matrix is

$$S_{CZ}(g) = \begin{pmatrix} 1 & 0 & 0 & 0 \\ 0 & 1 & 0 & 0 \\ 0 & g & 1 & 0 \\ g & 0 & 0 & 1 \end{pmatrix}.$$

The graph associated with the graph states identifies edges as CZ gates applied between nodes, which are the squeezed modes, weighted with g.

To simplify the many degrees of freedom present in our networks, for the moment we shall assume that all the nodes will be squeezed in $\hat{p}$ by s and all the edges have a correlation strength of g. If we apply a CZ gate network with adjacency matrix A to a multimode squeezed vacuum σ_s, with squeezing factor s we obtain a Gaussian network with covariance matrix [33]

$$\begin{aligned} \sigma &= \begin{pmatrix} \sigma_{qq} & \sigma_{qp} \\ \sigma_{pq} & \sigma_{pp} \end{pmatrix} = \begin{pmatrix} \mathbb{1} & 0 \\ A & \mathbb{1} \end{pmatrix} \sigma_s \begin{pmatrix} \mathbb{1} & A \\ 0 & \mathbb{1} \end{pmatrix} \\ &= \begin{pmatrix} R\mathbb{1} & RA \\ RA & RA^2 + \mathbb{1}/R \end{pmatrix}, \end{aligned} \tag{5}$$

where $R = 10^{s/10}$. The $2N \times 2N$ covariance matrix σ is divided in four $N \times N$ blocks, where the blocks σ_{qq} and σ_{pp} represent the correlations among the different nodes' q- and p-quadratures, respectively, whereas the blocks σ_{qp} and σ_{pq} describe the correlations between q- and p-quadratures.

Bear in mind that the CZ-gate operations that theoretically identify the edges of the networks are seldom realized in any laboratory, being very challenging to accomplish. What is commonly done, as explained in the previous subsubsection, is the reduction of the covariance matrix of the graph state in (5) to the form of Eq. (3), which is also a recipe for building the graph states from a certain number of squeezed modes (Δ) and linear optics transformations (O).

Our model aims at reproducing the existing photonic platforms [7,8,10,14] with realistic experimental constraints, such as a limited amount of squeezing, but without taking into account propagation losses. This work is focused on the capabilities of pure CV quantum states to act as quantum networks and the resources needed for their generation. Generation losses can be very low, so the hypothesis of pure states is a realistic one, whereas propagation losses can be mitigated by considering local (short distances) networks, and their effect on long distances will be included in future works. At the same time, we probe the capabilities of photonic platforms while the scaling of the network increases beyond the capacities allowed by state-of-the-art technology.

[1]While usually the name cluster is used when the graph shape allows for universal quantum computing, in this work we will use the terms cluster state and graph state as synonyms.

III. COST OF QUANTUM NETWORKS

Gaussian bosonic states are of particular significance in the theory of CV quantum information. They are in fact resources for measurement-based quantum computing [30,32], quantum simulations [11], multiparty quantum communication [7,34], and quantum metrology [35,36]. Furthermore, their graphical structure simplifies their study through *graphical calculus*, a formalism introduced by Menicucci, Flammia, and van Loock [31]. Some elements of graphical calculus are summed up in Appendix D.

The correlations between the quadrature measurements of Gaussian states are fully described by their covariance matrix σ. Therefore, as usual in the literature, we will not further mention the first moments, which describe only a deterministic shift of the measurements which can easily be compensated when known and are therefore irrelevant.

Through the Bloch-Messiah decomposition (see Sec. II A), one can see that the eigenvalues $\lambda_i^{\pm}$ of the covariance matrix σ represent the squeezed and antisqueezed variances of the uncoupled oscillators, e.g., the uncertainty of measuring the real and imaginary part of the electromagnetic field. Together they form the *squeezing spectrum*. The first result of this paper is the following analytical relation between the squeezing spectrum of the Gaussian state and the adjacency spectrum of the graph:

$$\lambda_i^{\pm} = \tfrac{1}{2}\left(1 + D_i^2/2 \pm \sqrt{D_i^2 + D_i^4/4}\right), \tag{6}$$

where D_i are the eigenvalues of the adjacency matrix A. Equation (6) shows the interplay between the physical resources necessary to experimentally implement a CV graph state and the spectrum of the underlying graph. This implies that we can use spectral graph theory to characterize analytically the physical requirements of building Gaussian networks and thus predict which one will be easier to realize. A first crucial consequence is that different graph states whose underlying graphs are cospectral, e.g., their adjacency matrices have the same eigenvalues, can be transformed into each other applying passive linear optics.[2] The intrinsic connection between the squeezing of a Gaussian network and its topology was already put in evidence in the limit of large squeezing by Gu *et al.* [32], who showed a relation between the squeezing required to produce a CV graph state and the singular value decomposition of the associated adjacency matrix. Our result is a generalization of Theorems 2 and 3 of Ref. [32], exact and valid for finite squeezing, i.e., in a regime accessible with current technology.

Another crucial consequence of Eq. (6) is that for CV graph states the number of independent squeezed modes in their Bloch-Messiah decomposition corresponds to the rank $\mathrm{rk}(A)$ of the associated adjacency matrix A. This immediately translates into the number of squeezers needed to construct said state.

Squeezing is the essential resource for building Gaussian entangled states. A natural question is thus: what is the

[2]In general, any CV graph can be reshaped in any other graph via a symplectic transformation; in this case, it is an orthogonal transformation, and its physical realization involves only linear optics without any supplementary squeezing.

squeezing cost of producing a quantum state? A general resource theory for Gaussian states is provided by Lami *et al.* [37], with the specific case of squeezing described in [38], where Idel, Lercher, and Wolf find an operational squeezing measure, *the squeezing cost*. Its expression for any pure[3] Gaussian state of covariance matrix σ is

$$G : \mathbb{R}^{2N\times 2N} \to \mathbb{R}, \quad G(\sigma) = \sum_{i=1}^{N} 10\log_{10}[2\lambda_i^+(\sigma)], \tag{7}$$

where we chose to express it in dB.

We employ this to classify network topologies, depending on the scaling of their squeezing cost with the size of the network. In the rest of the paper (unless explicitly specified), we will consider an initial set of N modes vacuum states with no initial squeezing ($s = 0$), as it can be easily proved that initial uniform squeezing only adds a constant factor to the final squeezing cost. We also assume that the CZ-gate coupling strength $A_{ij} = g = 1$ for every edge of the graph, keeping the effects of nonuniform correlations for future works.

Notice that there is also a simple relation between the adjacency matrix A of a graph state and the mean energy difference between the state and the vacuum. Assuming that the energy E of the state is the mean value of the harmonic oscillator Hamiltonian on the state

$$E = \langle \hat{H}_{HO}\rangle = \frac{\hbar}{2}\sum_i \omega_i\left(\langle \hat{x}_i^2\rangle + \langle \hat{p}_i^2\rangle\right) = \frac{\hbar\omega}{2}\mathrm{Tr}(\sigma), \tag{8}$$

where we also assumed that all the modes have the same frequency $\omega_i = \omega$. From this, we can write

$$\Delta E = E - E_0 = \frac{\hbar\omega}{2}\mathrm{Tr}(\sigma - \sigma_0) = \frac{\hbar\omega}{2}\mathrm{Tr}(A^2). \tag{9}$$

The quantity on the right-hand side is proportional to the second moment of the eigenvalues distribution, and it sets a fundamental lower bound on the energy necessary to implement such states. From a topological point of view, the trace of the nth power of the adjacency matrix equals the number of closed loops of length n on the graph [39]. Thus, for $n = 2$, it corresponds to the number of edges in the network and implies that each independent application of the CZ gate adds the same amount of energy. A resource scaling that is linear with the number of edges in the network is typical of DV networks (i.e., DV graph states), where each new edge requires a new Bell pair. The scaling of the squeezing in CV networks with the size of the network, as we have seen, depends instead on the structure of the underlying graph and can be nonlinear with the number of edges. We want to stress here that squeezing—and not energy—is the technologically nontrivial enabling resource to be implemented for building the CV networks. If we look again at the example of the star and the diamond graph, the number of edges in the two graphs is different, hence they would have different energies. As they have the same number of squeezed modes, we can transform one into the other with passive optics, e.g., without spending energy or changing the squeezing cost. However, it has to be clarified that the two main squeezed modes for the diamond have larger eigenvalues than the star network. Thus, if we transform a star graph into a diamond with linear optics, it would be equivalent to a graph state obtained by the application of CZ gate with a weaker coupling g. But again this behavior is accounted for by the squeezing cost, which is the relevant quantity in designing CV networks.

In the following, we will consider an initial set of N modes vacuum states with no squeezing ($s = 0$), as it can be easily proved that initial uniform squeezing only adds a constant factor to the final squeezing cost. We also assume that the CZ-gate coupling strength $g = 1$ for simplicity; however, the analytical results we provide apply also in the general case.

A. Regular networks

Let us first discuss some regular network structures. We shall consider the following topologies:

(i) The *linear graph* $\mathcal{L}_N$, with N nodes and $N - 1$ edges, is accomplished by connecting each node in series to the next:

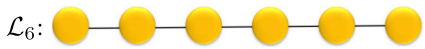

(ii) The *ring graph* $\mathcal{R}_N$, with N nodes and N edges, is a linear graph with a closed loop:

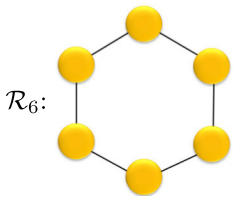

(iii) In the *star graph* topology $\mathcal{S}_N$, with N nodes and $N - 1$ edges, every peripheral node is linked to a central node, called a hub:

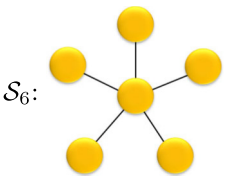

(iv) The *diamond graph* $\mathcal{D}_N$, with N nodes and $2(N - 2)$ edges, has two hubs, each linked to all the $N - 2$ central nodes of the network. It is isomorphic to the complete bipartite graph in which one of the subsets has two nodes and the other has $N - 2$ nodes:

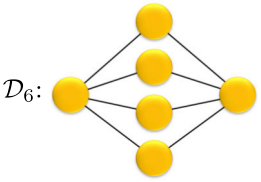

[3]The more generic expression for mixed states is slightly more involved: $G(\sigma) = -\sum_{i=1}^{N} 10\log_{10}[\max(2\lambda_i^-(\sigma), 1)]$. For pure Gaussian states, i.e., all the states considered in this work, this expression is equivalent to Eq. (7) because $\sqrt{\lambda_i^+\lambda_i^-} = \frac{1}{2}$.

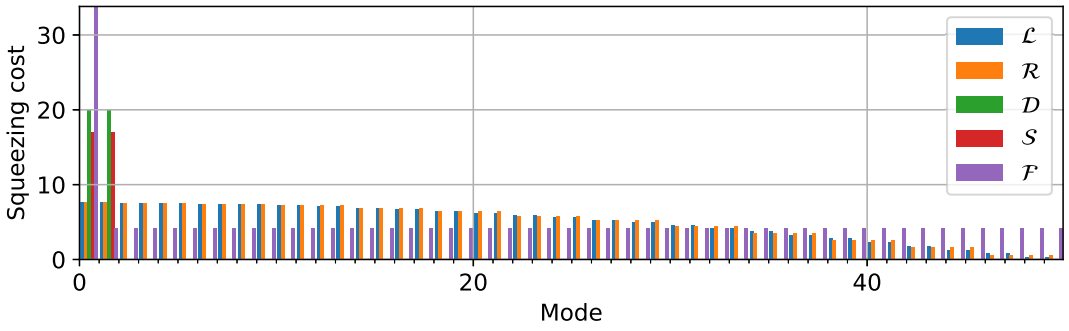

FIG. 1. Squeezing cost distribution, measured in dB, for regular networks. For each mode, the networks are ordered as linear $\mathcal{L}_N$, ring $\mathcal{R}_N$, star $\mathcal{S}_N$, diamond $\mathcal{D}_N$, fully connected $\mathcal{F}_N$ networks in the $N = 50$ modes, $s = 0$, $g = 1$. All the networks present some squeezing in each mode except the $\mathcal{S}$ and $\mathcal{D}$, which have an equal amount of squeezing only in the first two modes. The $\mathcal{F}$ network has a large peak of squeezing in the first mode, while the remaining amount of squeezing is equally distributed in the other modes.

(v) In the *complete* (or *fully connected*) *graph* $\mathcal{F}_N$, with N nodes and $\frac{N(N-1)}{2}$ edges, all nodes are interconnected:

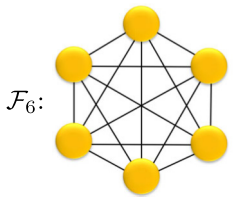

Let us first take a look at the full squeezing spectrum of these topologies for a fixed number of nodes $N = 100$. This is shown in Fig. 1, where the values were computed starting from the adjacency matrix spectrum of regular graphs [40]. We can see that, as expected, the linear and the ring graphs have a very similar spectrum, with small deviations induced by the periodicity of the latter that becomes negligible for large N. The star and the diamond networks have only two identically squeezed modes for all N. They are thus cospectral up to a factor and can be transformed into each other with linear optics. Finally, the fully connected graph has one large eigenvalue that grows with N and $N - 1$ equal eigenvalues, independent of the size of the graph. These eigenvalues are computed analytically by diagonalizing the adjacency matrix A and using Eq. (6) in Appendix B.

Let us now see how the total squeezing cost $G(\sigma)$ scales with the number of nodes N for each of the network topologies presented above. This scaling is computed analytically using Eq. (7) in Appendix B. In Fig. 2 we can see how the linear and the ring graphs are superposed, sharing the same squeezing cost per node that, as shown in Appendix B, is constant with N. The cost of the star and diamond grows logarithmically with N and in both cases has a simple expression and presents the lowest cost among the regular graphs we studied. In all these cases, although the actual squeezing cost would be smaller for these networks, the amount of squeezing required in each mode is much larger, so, depending on the experimental scenario, their implementation could be the easiest or the most challenging from an experimental point of view. In any case, these networks have interesting applications for quantum communications. In particular, the star graph can be used for secret sharing [7], while the diamond produces an effect that we call *parallel enhancement of entanglement*, which will be explained in the next section. Finally, the fully connected graph has a cost that grows linearly with N and, despite having the largest number of edges and thus squeezing increasing operations, for a large number of nodes is slightly cheaper than the linear graph.

A relevant application of these results would be to minimize the experimental difficulty—modeled by the squeezing cost and/or the number of squeezers—to prepare the Gaussian graph states used as resources for universal quantum computation. To our knowledge, all such proposals rely on 2D-lattice structures [30,32], similar to the ones proved to be necessary for DV measurement-based quantum computation [41]. We show in Appendix B the squeezing cost of a D-dimensional cubic lattice to scale linearly with the number of qumodes they contain. We conjecture the same proportionality holds for any D-dimensional regular lattice. Furthermore, we conjecture this cost is proportional to the number of qubits used for the equivalent DV measurement-based quantum computation [41], which is itself proportional to the spacetime complexity of the corresponding quantum computation in the circuit model.

B. Complex networks

In the previous section, we described graphs that are built through a deterministic algorithm, though we can also con-

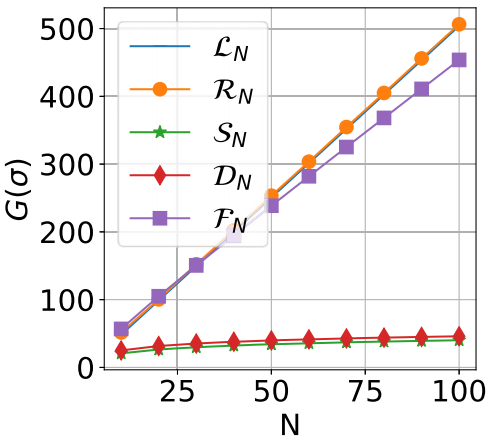

FIG. 2. Trend of the squeezing cost $G(\sigma)$, measured in dB, for the regular topologies: linear $\mathcal{L}_N$, ring $\mathcal{R}_N$, star $\mathcal{S}_N$, diamond $\mathcal{D}_N$, fully connected $\mathcal{F}_N$ networks for $N = 100$ nodes.

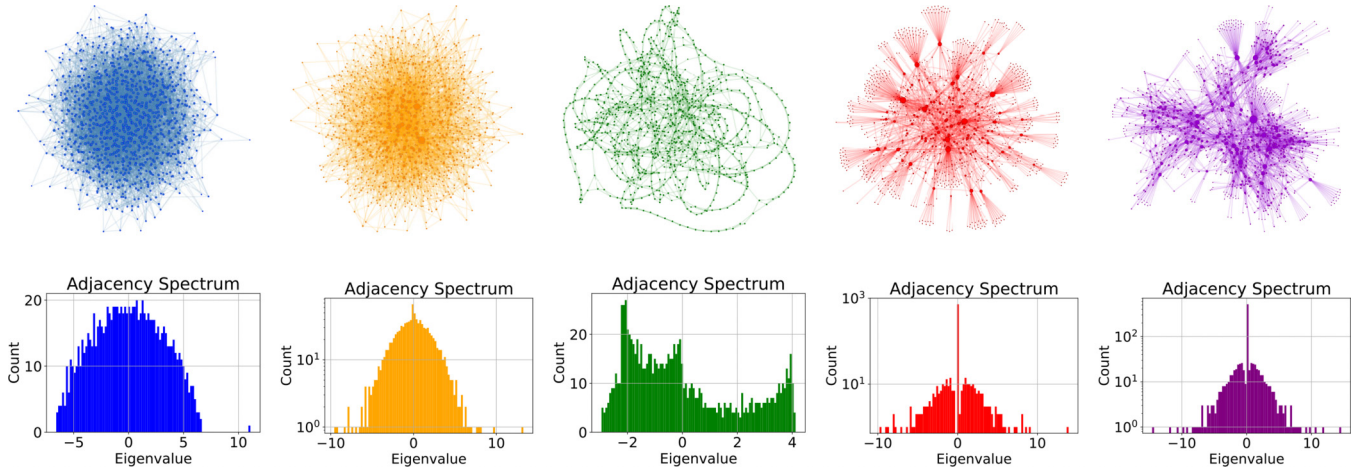

FIG. 3. Some complex networks and their adjacency matrix eigenvalues distribution for $N = 1000$ nodes: (a) Erdős-Rényi (ER) $\mathcal{G}_{ER}$ $\mathrm{rk}(A_{\mathcal{G}_{ER}}) = 1000$, Barabási-Albert $\mathcal{G}_{BA}$ $\mathrm{rk}(A_{\mathcal{G}_{BA}}) = 997$, (c) Watts-Strogatz $\mathcal{G}_{WS}$ $\mathrm{rk}(A_{\mathcal{G}_{WS}}) = 1000$, (d) AS internet $\mathcal{G}_{AS}$ $\mathrm{rk}(A_{\mathcal{G}_{AS}}) = 278$, and (e) proteins interaction $\mathcal{G}_{PP}$ $\mathrm{rk}(A_{\mathcal{G}_{PP}}) = 492$. In the distributions of the BA, AS, and PP the y axis is in log scale.

struct a graph based on statistical models [42,43]. This is the difference between the regular networks of the previous section and the random networks shown in Fig. 3. An exemplary standard for random networks is the Erdős-Rényi (ER) model $\mathcal{G}_{ER}(N, p)$, in which each pair of the N nodes have a probability p to be linked; the network thus has $\binom{N}{2}p$ edges on average [44].

Most natural networks cannot be described by regular or random graphs. A branch of research, called complex networks, studies these networks. Complex networks have unique topological features not found in regular or random graphs and resemble real-world systems [45]. One important class of complex networks is the "small world" network. These networks have short average path lengths and high clustering. The Watts-Strogatz model $\mathcal{G}_{WS}(N, Q, \beta)$ exemplifies these properties. It starts as a regular periodic graph with N nodes and Q neighbors per node. With probability β, edges are rewired to other nodes, avoiding self-loops and duplicates. Another class is "scale-free" networks with "long-tailed" structures. They follow a power-law degree distribution, $P(k) \propto k(-\gamma)$, unlike regular and Watts-Strogatz models. The Barabási-Albert model $\mathcal{G}_{BA}(N, K)$ captures this behavior and emulates network growth and preferential attachment. "Technological networks" are designed for resource distribution, like the internet autonomous system (AS) $\mathcal{G}_{AS}(N)$. To study AS topology, reference work by Elmokashfi *et al.* [46] is used. Complex networks also appear in nature, including various "biological networks." One example is the protein-protein interaction network model $\mathcal{G}_{PP}(N, \sigma)$ from Ref. [47].

Complex networks are important in many natural and technological systems [45]; similarly CV graph states with complex network shapes are particularly relevant for simulating quantum complex networks environments [11,48] and to study future quantum information and communication networks mimicking the structure of the classical communication networks. It is then worth studying the scaling of the necessary squeezing resources for their implementation. In Fig. 4 we show the squeezing cost distribution for the various topologies of complex networks by showing the squeezing cost of all the principal modes. Notice that, since complex networks are a subset of correlated random networks, the set of eigenvalues of the adjacency matrix is not deterministic. However, the eigenvalues follow a probability distribution $f(x)$, well known in some selected cases [49], which allows us to derive the expected value of the total squeezing cost as

$$\langle G(\sigma)\rangle = 10N \int f(x) \log_{10}[\lambda^{(+)}(x)]\, dx, \tag{10}$$

where $\lambda^{(+)}(x)$ is the largest eigenvalue deduced from Eq. (6) and x indicates the corresponding mode. This gives us a straightforward recipe to compute G from the distribution f. Furthermore, it allows us to deduce the scaling of G from the distribution of the eigenvalues and especially from the width of this distribution. If the distribution does not change with N, then G scales linearly with N, whereas any growth in the width of f would imply a superlinear scaling of G.

In Fig. 5 we report the trend of the total squeezing cost as a function of the number of nodes for each of the above complex topologies. In this case, the networks were simulated and the values obtained were averaged over ten different samples.

From the plots, we notice that the linear trend is the most common case. The spectral theory of real graphs is a much less established field, and there is only a handful of results we can apply to make predictions. In particular, to the best of our knowledge, there are only empirical results about the convergence of the spectral density for the scale-free and the small-world models. In Ref. [49], however, Farkas *et al.* show some crucial properties of the spectra of scale-free and small-world graphs, although further studies are required to have a deeper insight into the properties of complex quantum graph states. In particular, it is shown that, fixing the other network's parameters, the width of their distribution is constant with N, implying as we discussed a linear trend of G, consistent with the observed one.

The protein-protein [47] and AS networks, which are scale-free networks, have the additional property of having many nodes sharing the same neighborhood, which implies a large kernel of their adjacency matrix and thus a slower growth of G compared to the other complex graphs, which are essentially full rank. More specifically, the low rank of the protein-protein

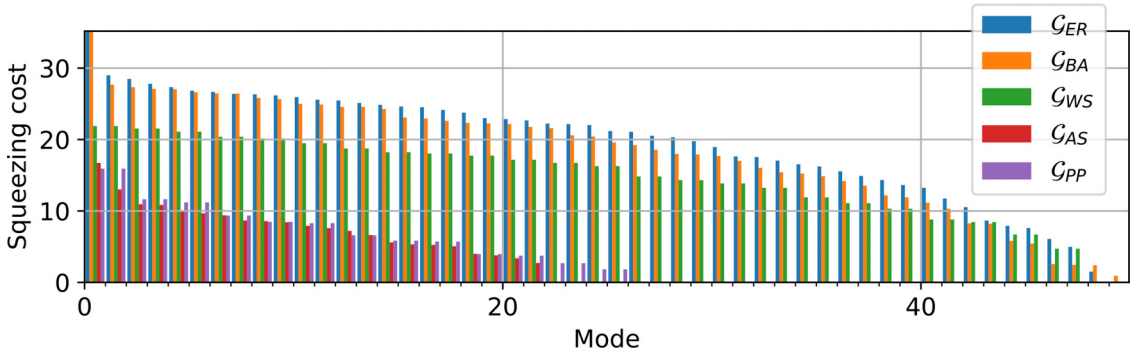

FIG. 4. Squeezing cost distribution, measured in dB, for complex topologies. For each mode, the networks are ordered as Erdős-Rényi $\mathcal{G}_{ER}$, Barabási-Albert $\mathcal{G}_{BA}$, Watts-Strogatz $\mathcal{G}_{WS}$, AS internet $\mathcal{G}_{AS}$, and protein-protein interaction $\mathcal{G}_{PP}$ networks in the $N = 50$ modes.

interaction graph of Ispolatov, Krapivsky, and Yuryev [47] is explained by the duplication process at the heart of its generation, which, by definition duplicates the neighborhood of vertices. For the AS graph, a model of the internet by Elmokahfi, Kvalbein, and Dovrolis [46], many of the nodes are leaves (clients) connected to a few client providers. This results in a very low, but still linearly increasing with N, rank, explaining why its squeezing cost is the lowest of the line in Fig. 5.

The anomalous superlinear trend of the ER model is a direct consequence of the same theory. As we show in Appendix C, this $N \log N$ scaling is due to the widening with N of the Wigner semicircular law [50] followed by the ER graph.

Now that we have characterized the cost of implementing Gaussian quantum networks, we will describe how to use them as a substrate to perform quantum communications.

IV. ROUTING ENTANGLEMENT

Quantum entanglement is a paramount resource for quantum information purposes. In particular, bipartite entanglement represents the fundamental requirement that a shared quantum channel should have to enable a truly quantum teleportation. In the framework of quantum communications, the networks previously described can be seen as distributed Gaussian *quantum teleportation networks* [51], where each pair of nodes can employ the preestablished quantum correlations together with *Local Operations* and *Classical Communications* (LOCC) to teleport a Gaussian quantum state from one node to the other.

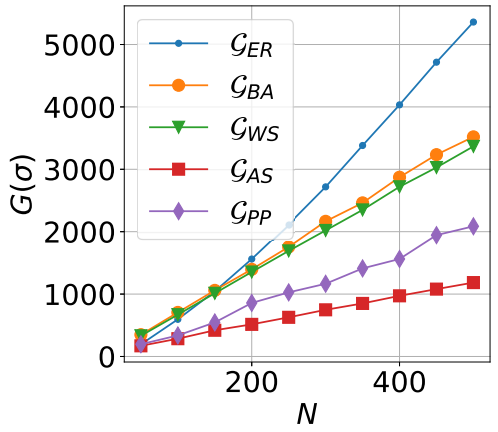

FIG. 5. Trend of the squeezing cost, measured in dB, for complex topologies: Erdős-Rényi $\mathcal{G}_{ER}$, Barabási-Albert $\mathcal{G}_{BA}$, Watts-Strogatz $\mathcal{G}_{WS}$, AS internet $\mathcal{G}_{AS}$, and protein-protein interaction $\mathcal{G}_{PP}$ networks up to $N = 500$ nodes.

A typical approach of quantum networking and routing consists of distributing photonics states like single photons, Bell pairs, or Gaussian states and then use synchronous local operations that build the wanted entanglement structure between the agents [3,52–60]. We remark that our type of communication quantum networks is inherently different from the typical qubit networks that are currently being deployed in different metropolitan areas [61]. In those cases, for example, each entanglement link is pairwise between two qubits, and as a consequence each node of the network will have to receive, store, and measure as many quantum states as it has neighbors. Conversely, in a Gaussian quantum network, the same qumode can be entangled with an arbitrary number of other nodes. Moreover, the production of such states, their manipulation to increase the entanglement among two nodes, and their measurement to perform quantum teleportation can be achieved deterministically, unlike the discrete variables case. Nonetheless, qubits networks have been extensively studied over the past years, whereas Gaussian teleportation networks are a very recent emerging field. Our purpose is, thus, not to prove the superiority of the latter, but rather to explore its properties and the differences from the DV schemes to get the best of both worlds.

We consider the case where a preexisting CV multipartite entangled state is distributed among the players and then local operations reconfigure the entanglement connections, similarly to some protocol in the DV case [62]. The choice is motivated by the fact that multimode entangled states can be directly generated via an optical platform [6,8–10,20], and their shape can be easily manipulated [7,11].

In our framework, if two nodes A and B need to teleport a quantum state, they can be helped by the other nodes in the network that will perform a quadrature measurement in one of the two complementary canonical variables $\hat{q}$ or $\hat{p}$ to increase the strength of the entanglement in the final pair. In a naive strategy, the teleportation between two arbitrary nodes can be implemented simply by ignoring all the other nodes and exploiting the residual bipartite entanglement together with classical communications. This strategy is a direct extension

of the standard teleportation protocol from two to more stations and is called *nonassisted* protocol [63].

Another set of strategies is based upon cooperative behavior, where all the other nodes assist the teleportation between the chosen pair (Alice and Bob) using LOCC. If the external nodes perform suitable local measurements and then classically communicate their outcomes to Bob, the latter can use this additional classical information to improve the process via modified conditional displacements. These strategies are called *assisted* protocols and are the ones that determine what we call routing protocol in this article.

According to Gu *et al.* [32] quadrature measurement on a mode of a Gaussian network like the ones we considered so far can be described by two simple rules:

(1) *Vertex Removal:* a $\hat{q}$-measurement on a qumode removes it from the network, along with all the edges that connect it.

(2) *Wire Shortening:* a $\hat{p}$-measurement on a qumode is just a $\hat{q}$-measurement after a Fourier transform, which corresponds to a phase rotation of $\pi/2$: $S_F = S_R(\theta = \frac{\pi}{2})$. The node will thus be removed, but the phase shift will induce correlations between the neighboring edges. Thus, measurements in the momentum basis allow us to effectively shorten linear graph states.

These rules are exposed more formally in Appendix D, using the graphical calculus introduced by Menicucci, Flammia, and van Loock [31].

If two nodes A and B need to teleport a quantum state, they can be helped by the other nodes in the network that will perform these operations to increase the strength of the entanglement in the final pair. A typical measure of entanglement is the *logarithmic negativity* [17–19,64]

$$\mathcal{N} = -2\log_2 \tilde{\nu}_-, \tag{11}$$

where $\tilde{\nu}_-$ is the smallest symplectic eigenvalue of the partially transposed covariance matrix of the pair. Partial transposition is a necessary operation for the positive partial transpose (PPT) criterion [65] and is easily implemented in Gaussian states by changing the sign of the momentum of one of the two subsystems.

The symplectic eigenvalues $\nu_\pm$ of a two-mode system can be computed through the invariants of the covariance matrix [64]. More specifically, we can define the *seralian*

$$\Delta = \det\sigma_A + \det\sigma_B + 2\det\sigma_{AB}, \tag{12}$$

where σ_A and σ_B are the local covariance matrices of the single-mode subsystems A and B, and σ_{AB} represents their correlations. From this, we can compute the symplectic eigenvalues as

$$\nu_\pm^2 = \frac{\Delta \pm \sqrt{\Delta^2 - 4\det\sigma}}{2}. \tag{13}$$

A. Regular networks

In Fig. 6 we compare the effect of different regular topologies of quantum networks to distribute entanglement between two of the farthest nodes inside the network.

For each regular network topology, we employ the optimal measurement strategy to maximize the entanglement. The simplest cases are the *star* and *complete* networks. In the first case the best *assisted* strategy is to let everyone perform a $\hat{q}$-measurement on their node except the central one, which will make a *wire shortening* to link the final pair. In the complete network, A and B are already linked by an edge, so it is sufficient to measure the position in all the other qumodes (notice that this strategy outperforms the nonassisted protocol). In both these cases, the entanglement is constant with the number of nodes in the network as we would expect, and the wire shortening of the central node in the star graph decreases the logarithmic negativity with respect to the complete graph [66]. In the linear graph, all the nodes have to wire shorten from A to B. Here the logarithmic negativity quickly decreases with the number of nodes.

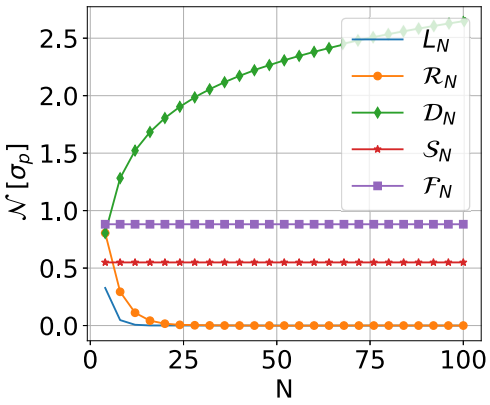

FIG. 6. Logarithmic negativity in the final two modes states after all the other agents have locally measured their node for the regular topologies: linear $\mathcal{L}_N$, ring $\mathcal{R}_N$, star $\mathcal{S}_N$, diamond $\mathcal{D}_N$, fully connected $\mathcal{F}_N$ networks up to $N = 100$ nodes.

The decrease of entanglement with the size of the network seems to be typical in all configurations except the diamond graph, where all the central nodes are $\hat{p}$-measured. This behavior is quite counterintuitive and might be expected to increase the fidelity of quantum communications. We show in Appendix E that the lowest symplectic eigenvalue of the partially transposed covariance matrix for this system goes like

$$\left(\tilde{\nu}_-^{(\mathcal{D}_\mathcal{N})}\right)^2 = \frac{1}{1+2NRg^2}, \tag{14}$$

where $R = 10^{s/10}$ is the inverse of the squeezing in $\hat{p}$, with squeezing factor s in dB. Hence, the logarithmic negativity grows logarithmically with NRg^2,

$$\mathcal{N}^{(\mathcal{D}_\mathcal{N})} = \log_2(1+2NRg^2), \tag{15}$$

and the two modes become perfectly correlated in the limit of either infinite squeezing, infinite strength CZ gate, or infinitely many nodes in the network.

B. Complex networks

We present a naive entanglement routing protocol that takes into account some of the properties studied in the previous section (notably, the parallel enhancement of entanglement), and we will apply it to complex topologies to show that the enhancement of the entanglement with respect to the trivial protocol is, in principle, easily achievable. Imagine we

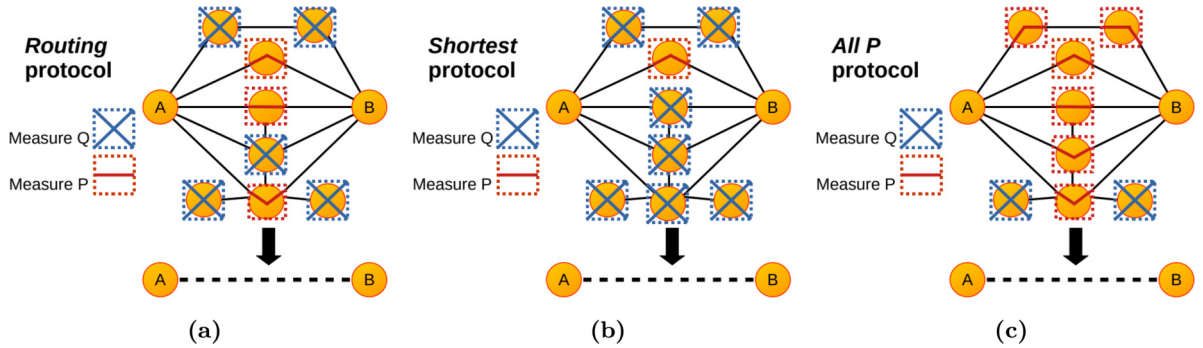

FIG. 7. Scheme of the three protocols for the entanglement distribution: (a) the *Routing* protocol takes a list of the shortest paths connecting A and B and measures in $\hat{p}$ those that increase the logarithmic negativity while the rest is measured in $\hat{q}$; (b) the *Shortest* protocol considers only one of the shortest paths to be measured in $\hat{p}$ and the rest in measured in $\hat{q}$; (c) the *All P* measures the nodes with only one connection in $\hat{q}$ and all the rest in $\hat{p}$.

have a distributed network of entangled harmonic oscillators, where each node is honest and can perform classical communication and local homodyne measurement, and we want to establish an entangled pair between two nodes, Alice and Bob, that want to teleport a quantum state or perform quantum key distribution (QKD). The trivial protocol—called *Shortest* in the following—would be to find the shortest path between them and measure in $\hat{p}$ all the qumodes along this path and in $\hat{q}$ all the others. A careful look at the inner structure of the network, however, might help us increase the strength of the correlation. For example, if at any point, two nodes on the path are linked by multiple parallel routes, we can measure these in $\hat{p}$ to exploit the parallel enhancement of this diamond-like subnetwork.

To show this in practice, we test the performances of three different routing protocols (shown in Fig. 7) on various complex networks to establish a highly entangled pair [50]. We choose Alice to be one of the hubs of the graph and evaluate the efficiency of the protocol in delivering entanglement to all the other nodes. The quantum protocol that we propose to exploit the parallel enhancement of entanglement will be called simply *Routing*:

Routing: it takes as input the target node, Bob; it lists all the shortest paths connecting it to Alice and measures all the nodes that are not in these paths in the $\hat{q}$ quadrature, so that they will not influence the protocol. Among the list of paths, it checks one by one those to be measured in $\hat{p}$ to maximize the logarithmic negativity $\mathcal{N}$ of the final pair, while the rest will be measured in $\hat{q}$.

In the *Routing* protocol, in principle, we could have considered parallel paths of longer lengths that might have contributed to improving the logarithmic negativity. However, in practice, the only observed effect was the slowing of the performances while the entanglement was not increasing for all the cases we considered. The effect of the parallel paths can be appreciated when comparing the logarithmic negativity produced by *Routing* with that produced by *Shortest*:

Shortest: the difference of the latter is that it exploits only one of the shortest parallel paths, directly measuring everything else in $\hat{q}$.

In some cases the two protocols do not give a substantial difference, either because there are no parallel routes or because these do not help increase the entanglement; however, in many instances the effects of parallel routing are significant. The last protocol we compare with is *All P*:

All P: it measures in $\hat{q}$ all the terminal nodes of degree 1—the leafs—and the rest in $\hat{p}$.

This protocol is less effective than the first two but is always the quickest to simulate, whereas *Routing* can be computationally very slow on regular networks, which are characterized by long distances and many parallel paths, but becomes very efficient on complex sparse networks. The following simulations can be reproduced using our Python code, available at [50].

One instance of this program is given in Fig. 8, which shows the logarithmic negativity provided by the three different protocols for each node of an Autonomous System (AS) network [46] with 1000 nodes $\mathcal{G}_{AS}(N = 1000)$. At the beginning of the protocol, we pick Alice as the node, or one of the nodes, with the highest degree. The nodes are then sorted by their distance from Alice and, for the same distance, by the number of all the shortest paths connecting them to Alice. Additionally, the gray column represents the fraction of parallel paths useful to increase the entanglement. Notice that nodes at distance 1 cannot show any difference between the *Routing* and the *Shortest* protocols; however, many nodes at distance 2 present a greater logarithmic negativity than those at shorter distance after the *Routing*. This feature of quantum communication networks, e.g., that two nodes can benefit from improved communication if they are at a larger distance due to the parallel enhancement of entanglement, has no classical equivalent.

In Fig. 9 we show the graph of the network, where the nodes are again sorted by distance and number of parallel paths and the size of each node is proportional to its degree. In this figure, Alice is 0 and has a thick red contour. The

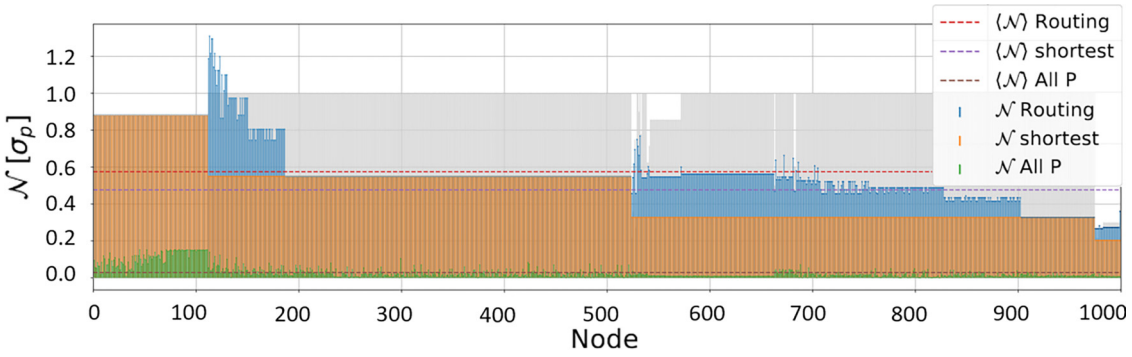

FIG. 8. Logarithmic negativity produced by the three different protocols applied to each node of the Autonomous System $\mathcal{G}_{AS}(N = 1000)$ network. The nodes are labeled in order of distance and of number of paths connecting to Alice. The blue (above), orange (middle), and green (below) stems represent the logarithmic negativity of the final pair after the *Routing*, *Shortest*, and *All P* protocols, respectively, while the dashed lines represent the mean value for all the nodes. The gray columns represent the ratio of paths that improved the entanglement in *Routing*, with respect to all the paths connecting A to B.

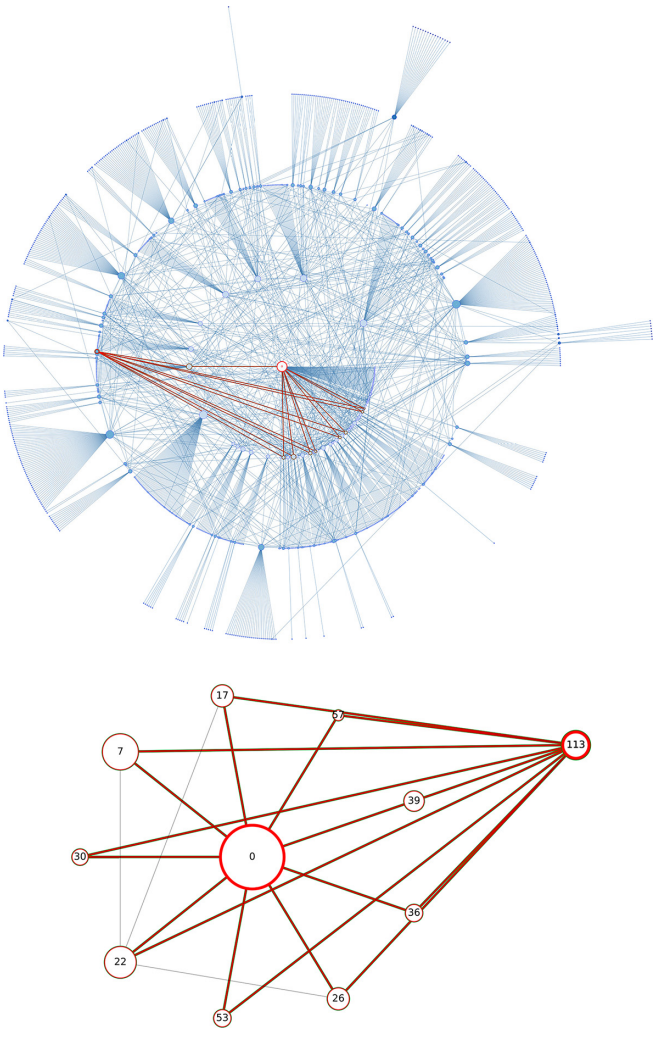

FIG. 9. Scheme of the $\mathcal{G}_{AS}(N = 1000)$ network on which we performed the protocol and subgraph of the paths connecting to the node with highest logarithmic negativity. The nodes are set in circles according to their distance from Alice, and their size is proportional to their degree.

node with the highest logarithmic negativity and all the paths that improved its entanglement are highlighted with red thick lines.

Appendix F presents the results of the same analysis we applied to other networks differing in size and topology, and for which we obtained different results.

V. CONCLUSION AND OUTLOOK

In this work we have investigated Gaussian multimode graph states with regular and complex topologies and studied their potential application for quantum communication protocols.

First, we have shown analytically and numerically that the cost of the networks is in general nonlinear with the number of edges and nodes and there are particular (regular and complex) graph shapes that optimize the cost and the number of squeezers over a number of nodes and edges in the networks. Among regular networks the diamond and the star graph need only two squeezed nodes to be built, independently from their number of nodes. Among the complex network shapes, the AS model is the most convenient in the number of needed squeezed states [46].

Then we studied the assisted teleportation protocol in Gaussian entangled networks, where a couple of nodes are assisted in the teleportation by local measurement in all the other nodes. This naturally defines a routing protocol in Gaussian networks. In particular, we have considered $\hat{q}$ and $\hat{p}$ homodyne quadrature measurements that allow respectively for vertex-removal and wire shortening. We showed analytically the effect of parallel enhancement of entanglement to improve the quality of quantum communication in the diamond network.

Finally, inspired by this quantum effect, we have devised a routing protocol that exploits wire shortening in parallel paths, and we have applied it to complex network graphs. The protocol named *Routing* is compared with *Shortest*, where wire shortening is done only in the shortest path, and *All P*, which removes all the terminal nodes while it wire shortens all the others. In most cases, the *Routing* improves the entanglement compared with *Shortest*. Also, in terms of computational

complexity, the *Routing* is much slower than *All P* in regular networks, where there are long distances between nodes and several parallel paths, but it is very efficient in complex sparse networks.

The devised *Routing* protocol is very general so that it can be applied to arbitrary networks, and it is particularly efficient for sparse not regular networks. Our simple graph exploration approach would be improved in computational efficiency by real graph-based algorithms, especially if we allow for approximate solutions [67]. Also, it would be interesting to allow for nonuniform distributions of squeezing s and CZ-gate strength g or more general homodyne measurements, i.e., going beyond the two $\hat{p}$ and $\hat{q}$ cases and considering measurements along $\hat{q}_\theta = \cos(\theta)\hat{q} + \sin(\theta)\hat{p}$. In addition, it could be interesting to examine a scenario in which the intermediate nodes are dishonest and do not cooperate to perform the routing, exploiting, for example, non-Gaussian operations. Finally the routing protocol has been implemented to solve the particular task of creating a perfect EPR pair between two nodes; future protocols will consider general reshaping in arbitrary multiparty states.

The numerical data that support the finding are available from the authors upon request and can be reproduced using the repository [50].

ACKNOWLEDGMENTS

We thank Dimitrios Tsintsilidas for the helpful discussions. This work is supported by the European Research Council under the Consolidator Grant COQCOoN (Grant No. 820079), by the European Union under the Project No. 101080174 CLUSTEC, by the French state from the Plan France 2030 managed by the Agence Nationale de la Recherche through the ANR-22-PETQ-0006 NISQ2LSQ and the OQuLus projects, by the ERC AdG CERQUTE, and by the Government of Spain (Severo Ochoa CEX2019-000910-S and TRANQI), Fundació Cellex, Fundació Mir-Puig, Generalitat de Catalunya (CERCA program).

The authors declare no competing financial or nonfinancial interests.

F.C. operated the numerical simulations and analyzed the data. All authors contributed to the theoretical analysis and to writing the manuscript. V.P. and F.C. supervised the work. V.P. conceived the project.

APPENDIX A: INTERPLAY BETWEEN SQUEEZING AND ADJACENCY SPECTRA

Consider an N-dimensional graph with adjacency matrix A. If we apply a set of CZ gates to the set of N modes of a vacuum state according to the edges defined by A, we end up with a Gaussian graph state with the following $2N$-dimensional covariance matrix:

$$\sigma = \frac{1}{2}\begin{pmatrix} \mathbb{1} & A \\ A & \mathbb{1} + A^2 \end{pmatrix}, \tag{A1}$$

where we assumed that the vacuum state variance is normalized to $1/2$. Since A is symmetric, it is always diagonalizable,

$$VAV^T = D = \mathrm{diag}(\{D_i\}), \tag{A2}$$

for some orthogonal matrix V, where $\{D_i\}_{i=1}^N$ is the set of the real eigenvalues of A. It follows that $VA^2V^T = VAV^TVAV^T = D^2$. Let us consider the following matrix:

$$W = \frac{1}{\sqrt{2}}\begin{pmatrix} V & V \\ V & -V \end{pmatrix}. \tag{A3}$$

We can verify easily that $WW^T = \mathbb{1}$, hence W is an orthogonal matrix implementing a basis change that would not change the spectrum of the matrix to which it is applied. If we apply it to σ we get

$$\sigma' = W\sigma W^T = \frac{1}{2}\begin{pmatrix} \mathbb{1} + D + D^2/2 & -D^2/4 \\ -D^2/4 & \mathbb{1} - D + D^2/2 \end{pmatrix}, \tag{A4}$$

which is a block matrix composed of diagonal matrices. We can permute the rows and columns of the matrix to get a diagonal block matrix

$$\Pi\sigma'\Pi^T = \bigoplus_{i=1}^{N} M_i, \tag{A5}$$

where Π is a permutation operator, while

$$M_i = \frac{1}{2}\begin{pmatrix} \mathbb{1} + D_i + D_i^2/2 & -D_i^2/4 \\ -D_i^2/4 & \mathbb{1} - D_i + D_i^2/2 \end{pmatrix}. \tag{A6}$$

In this basis, each block M_i represents a single-mode covariance matrix of a pure unentangled Gaussian state. We can hence diagonalize each block independently. In particular, notice that $\det(M_i) = \frac{1}{4}$, thus the eigenvalues of σ are given by

$$\begin{aligned} \lambda_i^{\pm} &= (\mathrm{Tr}(M_i) \pm \sqrt{\mathrm{Tr}(M_i)^2 - 4\det(M_i)}) \\ &= \tfrac{1}{2}\big(1 + D_i^2/2 \pm \sqrt{D_i^2 + D_i^4/4}\big). \end{aligned} \tag{A7}$$

These values represent the squeezed and antisqueezed variances of the uncoupled oscillators of Eq. (4), e.g., the uncertainty of measuring the real and imaginary part of the electromagnetic field. Equation (A7) shows the interplay between the physical resources necessary to experimentally implement a CV graph state and the spectrum of the underlying graph. This implies that we can use spectral graph theory to characterize analytically the physical requirements of building Gaussian networks and thus predict which one will be easier to realize. A first crucial consequence is that different graph states whose underlying graphs are cospectral, e.g., their adjacency matrices have the same eigenvalues, can be transformed into each other applying passive linear optics.[4] We will see later that the star and diamond networks have this property, making them a relevant class of Gaussian networks

[4]In general, any CV graph can be reshaped in any other graph via a symplectic transformation; in this case it is an orthogonal transformation, and its physical realization involves only linear optics without any supplementary squeezing.

for applications. The intrinsic connection between the squeezing of a Gaussian network and its topology was already put in evidence by Gu *et al.* [32], by proving a relation between the squeezing required to produce a CV graph state and the singular value decomposition of the associated adjacency matrix. Our result is an exact generalization of Theorems 2 and 3 of Ref. [32], beyond the limit of large squeezing, i.e., in a regime that is accessible with current technology.

Another crucial consequence of Eq. (A7) is that for CV graph states the number of independent squeezed modes (squeezers) in their Bloch-Messiah decomposition corresponds to the rank $\mathrm{rk}(A)$ of the associated adjacency matrix.

For any nontrivial graph, we have

$$2 \leqslant \mathrm{rk}(A) \leqslant N. \tag{A8}$$

The impossibility of rank 1 adjacency matrices comes from their null trace. If A is not full-rank, it has a non-null kernel. A common source of such kernel vectors is when one has k linearly independent sets $S_1, \ldots, S_k$ of vertices sharing the same neighborhood AS_1, where, by a slight abuse of notation, S_i denotes both a set of vertices and the corresponding column vector:

$$\forall 1 \leqslant i \leqslant k, \quad AS_i = AS_1. \tag{A9}$$

We have then

$$A \sum_{i=1}^{k} \alpha_i S_i = \left(\sum_{i=1}^{k} \alpha_i \right) AS_1, \tag{A10}$$

which is null if and only if $\sum_i \alpha_i = 0$. This gives us a null eigenspace of dimension $k-1$.

The most obvious example of this is the star graph, where $N-1$ vertices share the same neighbor, giving a null space of dimension $N-1-1 = N-2$, hence $\mathrm{rk}(A) = N-(N-2) = 2$. If one now looks at the complete $(k, N-k)$-bipartite graph, one easily finds two null eigenspaces of dimension $k-1$ and $N-k-1$. This leads to $\mathrm{rk}(A) = 2$. Any rank 2 graph is a complete bipartite graph, as can be shown by looking at A matrices one can build from two orthogonal vectors. Its two non-null eigenvalues of a rank-2 graph are

$$\pm D = \pm \sqrt{\frac{\mathrm{Tr}A^2}{2}} = \pm \sqrt{k(N-k)}. \tag{A11}$$

APPENDIX B: SQUEEZING SPECTRA OF REGULAR GRAPHS

Given any graph's spectrum we can employ Eq. (6) to compute the amount of squeezing in each mode required to build the Gaussian network. In the following calculations, we used the spectra of regular graphs known in the literature. A detailed reference on the spectra of regular graphs and how to obtain them can be found at [39,68].

Unlike energy, the squeezing cost has a nontrivial scaling with the number of edges, as can be seen in Fig. 10, where we plot the ratio between G and the number of edges in each regular network topology. In particular, the complete network shows the least squeezing cost per edge, having the largest number of edges.

We use the linear graph as a benchmark to see how the squeezing cost scales with the number of nodes and links.

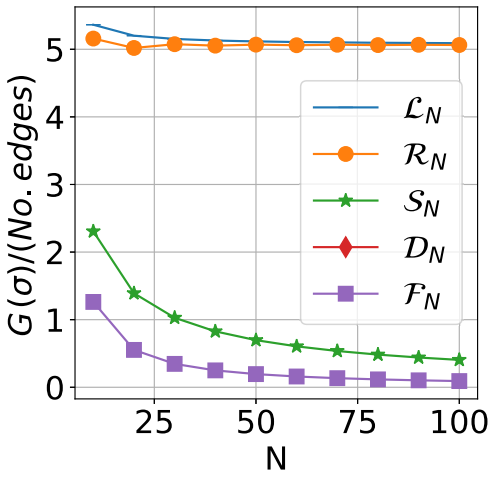

FIG. 10. Trend of the squeezing cost, measured in dB, divided by the number of edges in the network for the regular topologies: linear $\mathcal{L}_N$, ring $\mathcal{R}_N$, star $\mathcal{S}_N$, diamond $\mathcal{D}_N$, fully connected $\mathcal{F}_N$ networks for $N = 100$ nodes.

Single-mode squeezing and the CZ gate both require a fixed amount of squeezing to be implemented, so we would expect $G(\sigma)$ to scale linearly with the number of links and nodes. This is a direct consequence of the spectral distribution of the linear graph, which is

$$D_k(\mathcal{L}_N) = 2g \cos \frac{\pi k}{N+1}, \quad \{k = 1, \ldots, N\}. \tag{B1}$$

We can use Eqs. (6) and (7) to compute the squeezing cost exactly for any given N. For $N \gg 1$, the sum in Eq. (7) allowing us to compute the average squeezing cost per mode $\bar{G} = G/(\text{No. of squeezed modes}) = G/\mathrm{rk}(A)$ can be seen as a Riemann integral, which converges to

$$\bar{G} \simeq 10 \int_0^1 \log_{10} \left(1 + \frac{g^2 \cos^2 \pi y^2}{2} + \sqrt{g^2 \cos^2 \pi y + \frac{g^4 \cos^4 \pi y}{4}} \right) dy. \tag{B2}$$

This can be easily generalized to the case of a D-dimensional cubic lattice $\mathcal{L}_N^{(D)}$, considering that adding a new dimension would just add a new set of eigenvalues of the form (B1), as shown in Sec. 2.6 of [40]. As a consequence, the squeezing cost of the $\mathcal{L}_N^{(D)}$ is $G = O(N^D)$, whereas the average cost per mode would be again constant with the number of nodes N, as shown in Fig. 11.

Similarly, we can use the eigenvalue expression of the circular graph (or its generalization with $Q > 1$ nearest neighbors)

$$D_k(\mathcal{G}_{C_{(Q)}}) = g \frac{\sin[(Q+1)k\pi/N]}{\sin[k\pi/N]} - g, \quad k = \{0, \ldots, N-1\}. \tag{B3}$$

From this, we can see why the linear and circular graphs have the same scaling. In fact, for $Q = 1$, we have $D_k(\mathcal{G}_{C_{(Q)}}) = 2g \cos(k\pi/N) - g$.

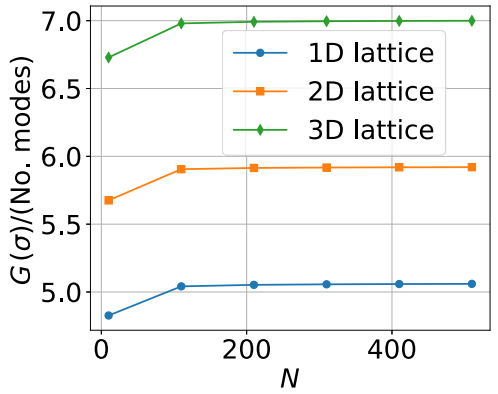

FIG. 11. Trend of the average squeezing cost per mode $\bar{G}(\sigma)$, measured in dB, for 1D, 2D, and 3D lattices, with N, N^2, and N^3 nodes, respectively. Notice that the cost becomes asymptotically constant, as predicted by the theory.

The spectra of the star and diamond graph have only two non-null eigenvalues [68]:

$$\{D_k(\mathcal{S}_N)\} = \left\{g\sqrt{N-1}, 0^{\otimes(N-2)}, -g\sqrt{N-1}\right\}, \tag{B4}$$

$$\{D_k(\mathcal{D}_N)\} = \left\{g\sqrt{2N}, 0^{\otimes(N-2)}, -g\sqrt{2N}\right\}. \tag{B5}$$

As a consequence, the cost of the star and diamond Gaussian networks grows logarithmically with N and has the following expressions:

$$G(\sigma_{\mathcal{S}_N}) = 20\log_{10} \times \frac{2-g^2+g^2N+\sqrt{g^4N^2-2(2g^4-g^2)N+g^4-4g^2}}{2} \tag{B6}$$

$$= 20\log_{10} N + 20\log g^2 + O\left(\frac{1}{N}\right), \tag{B7}$$

$$G(\sigma_{\mathcal{D}_N}) = 20\log_{10}(1+g^2N+g\sqrt{N(g^2N+4)}) \tag{B8}$$

$$= 20\log_{10} N + 20\log_{10} 2g^2 + O\left(\frac{1}{N}\right). \tag{B9}$$

Finally, the spectrum of the fully connected graph is

$$\{D_k(\mathcal{S}_N)\} = \left\{g(N-1), -g^{\otimes(N-1)}\right\}, \tag{B10}$$

yielding a squeezing cost that can be expressed as the sum of two contributions

$$G(\sigma_{\mathcal{F}_N}) = 10(N-1)\log_{10}\frac{2+g^2+g\sqrt{g^2+4}}{2} + 10\log_{10}\left[1+\frac{1+\sqrt{1+\frac{4}{g^2(N-1)^2}}}{2}g^2(N-1)^2\right] \tag{B11}$$

$$= 10(N-1)\log_{10}\frac{2+g^2+g\sqrt{g^2+4}}{2} + 20\log_{10} N + 20\log_{10} g + O\left(\frac{1}{N}\right), \tag{B12}$$

which sums up to a cost growing essentially linearly in N.

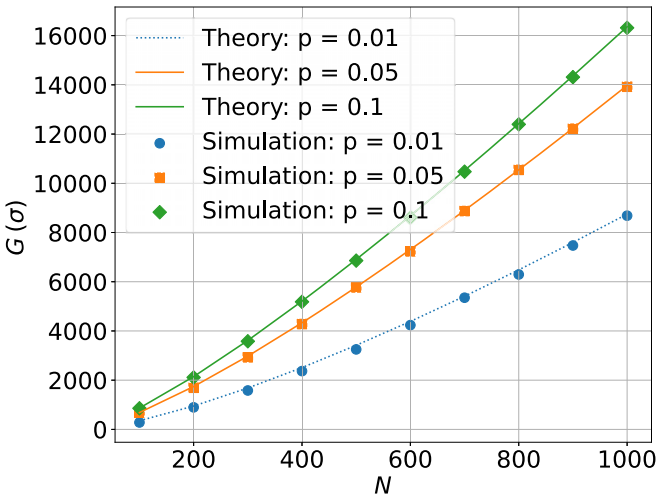

FIG. 12. Comparison between the theoretical prediction of Eq. (10) and the experimental numerical simulation of the squeezing cost, measured in dB, of the Erdős-Rényi graph state, for different values of p.

APPENDIX C: SQUEEZING SPECTRUM OF ERDŐS-RÉNYI GRAPHS

From Fig. 5 we notice that the most expensive growth belongs to the Erdős-Rényi (ER) topology, which is the only one among the topologies we studied whose trend is superlinear. This behavior is the easiest to predict from random matrix theory: the Wigner semicircular law for the distribution of the eigenvalues of a random graph [50] gives their probability distribution in the form $f(x) = f_{ER}(x) = \frac{2}{\pi R^2}\sqrt{R^2-x^2}$ [see Fig. 3(a)], where $R = 2g\sqrt{Np(1-p)}$, with a supplementary large eigenvalue D_1 such that $\lim_{N\to\infty} D_1/gN = p$, with probability 1. Casting it in Eq. (10) gives

$$\langle G(\sigma_{ER})\rangle = 10\log_{10}[2\lambda^+(gpN)] + \frac{40N}{\pi R^2}\int_0^R \sqrt{R^2-x^2}\log_{10}[2\lambda^+(x)]dx, \tag{C1}$$

where we used the parity of $f_{ER}(x)$, and the fact that the support is in $[0, R]$. Figure 12 shows the comparison between the theoretical behavior of the squeezing cost of the ER graph and the numerical experiments from the simulations. It shows a superlinear $\propto N\log N$ increase of the squeezing cost, which is explained by the widening of the support of f due to the increasing values of R. More formally, making the variable change $x = Ry$, we have

$$\log_{10}[2\lambda^+(Ry)] = 2\log_{10} R + \log_{10}\frac{y^2}{2} + O\left(\frac{1}{R^2y^2}\right). \tag{C2}$$

The second term in Eq. (C1) then becomes

$$\frac{40N}{\pi}\int_0^1 \sqrt{1-y^2}\log_{10}[\lambda^+(Ry)]dy = \frac{80N\log_{10}(R)}{\pi}\int_0^1\sqrt{1-y^2}dy + O(N) = 10N\log_{10}[g^2Np(1-p)] + O(N) \tag{C3}$$

and is the dominant term in the squeezing cost.

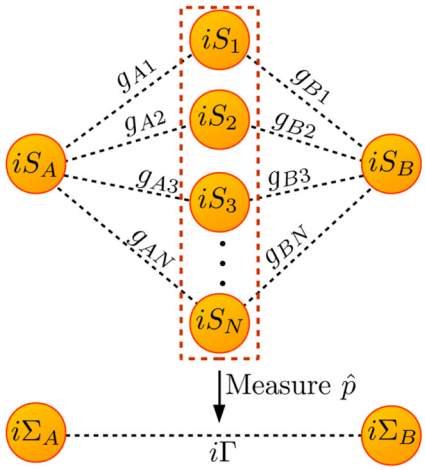

FIG. 13. Graphical representation of the diamond graph and its parallel enhancement of entanglement.

APPENDIX D: GRAPHICAL CALCULUS

In Ref. [31] Menicucci, Flammia, and van Loock provide a unified graphical calculus for all Gaussian pure states which is particularly suited for describing highly multimode Gaussian networks.

In this framework, an N-mode Gaussian state is completely described, up to displacements, by a $N \times N$ complex valued adjacency matrix:

$$Z = V + iU, \tag{D1}$$

where the real and imaginary parts of Z, V, and U, respectively, are related to the covariance matrix through the following unique decomposition:

$$\sigma = \frac{1}{2}\begin{pmatrix} U^{-1} & U^{-1}V \\ VU^{-1} & U + VU^{-1}V \end{pmatrix}. \tag{D2}$$

Gaussian graph states have a particular simple graphical representation, being

$$Z = A + iD, \tag{D3}$$

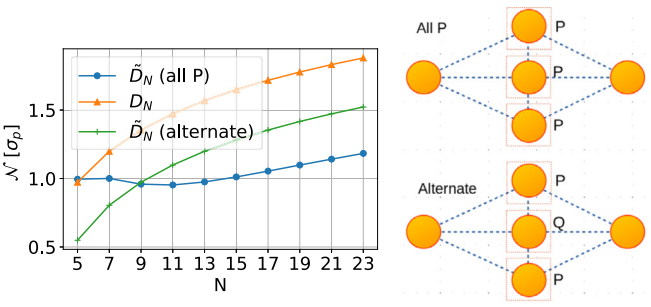

FIG. 14. Different measurement strategies for two types of diamond network: the standard $\mathcal{D}_N$ we have seen so far and the $\tilde{\mathcal{D}}_N$, in which the central nodes are connected to their neighbors. We apply two different strategies to $\tilde{\mathcal{D}}_N$: one is to measure all the central nodes in P, and the other is to alternate a p and a q measurement. We can see that measuring always in p is not necessarily the optimal strategy. On the right side, you can see a scheme of the $\tilde{\mathcal{D}}$ network and the two different measurement strategies.

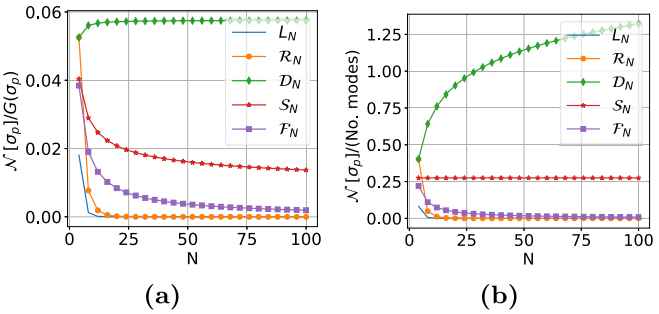

FIG. 15. Trend of the ratio between the logarithmic negativity of the final state and (a) the squeezing cost of the initial state, measured in dB, or (b) the total number of modes in the initial state for regular topologies: linear $\mathcal{L}_N$, ring $\mathcal{R}_N$, star $\mathcal{S}_N$, diamond $\mathcal{D}_N$, and fully connected $\mathcal{F}_N$ networks up to $N = 100$ nodes.

where A is the weighted adjacency matrix of the graph and D is a diagonal matrix that represents momentum squeezing, i.e., for $D = 10^{-2s/10}\mathbb{1}$ the momentum variance of all modes is reduced by $2s$ decibels.

All symplectic operations can be reproduced in this language; however, since we already know how to represent the resource graph states, we need only to implement the quadrature measurements in $\hat{x}$ and $\hat{p}$. We can express the state as

$$Z = \begin{pmatrix} t & R^T \\ R & W \end{pmatrix}, \tag{D4}$$

where the scalar t is the target mode we want to measure, $W \in \mathbb{R}^{(N-1)\times(N-1)}$ the subgraph of the untouched modes, and $R \in \mathbb{R}^{(N-1)\times 1}$ their correlations with the target mode. We have the following two rules:

(1) $Z \longrightarrow Z_q = W$ after a $\hat{q}$ measurement.

(2) $Z \longrightarrow Z_p = W - \frac{RR^T}{t}$ after a $\hat{p}$ measurement.

Thus, for a measurement in $\hat{q}$ we simply remove the node and its links from the graph, whereas for a measurement in $\hat{p}$ we also change the correlation between its neighbors, since $(RR^T)_{ij} \neq 0$ iff both i and j are in the node's neighborhood.

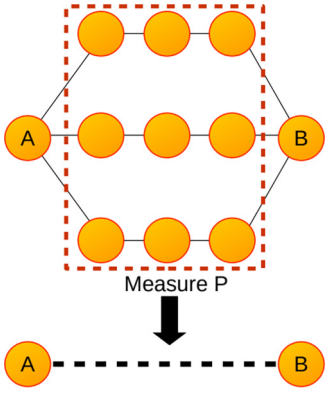

FIG. 16. Scheme of an entanglement routing protocol in a diamond chain with $K = 3$. All the central nodes are measured in P to concentrate entanglement between Alice and Bob.

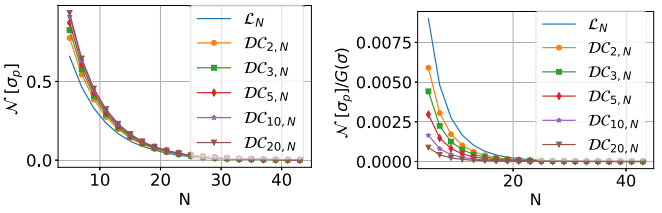

FIG. 17. (a) Trend of the logarithmic negativity of the output state for the diamond chain network, for various values of the number of branches K ($K = 1$ is the linear network). (b) Trend of the ratio between the logarithmic negativity of the final state and the squeezing cost of the initial state, measured in dB, for the diamond chains.

APPENDIX E: PARALLEL ENHANCEMENT OF ENTANGLEMENT

We can use the rules described in Appendix D to prove Eq. (14), which expresses analytically the power of parallel enhancement of entanglement in the diamond network when measuring the central nodes in $\hat{p}$. Let us assume that the nodes A and B are squeezed by a factor S_A and S_B, respectively, there are N central nodes, and the kth mode has squeezing S_k and is correlated with A and B through a CZ gate with strength g_{Ak} and g_{Bk}. It can then be easily shown that the final pair will have a purely imaginary adjacency matrix of the form

$$Z_{AB} = i\begin{pmatrix} \Sigma_A & \Gamma \\ \Gamma & \Sigma_B \end{pmatrix}, \tag{E1}$$

where $\Sigma_A = S_A + \sum_k \frac{g_{Ak}^2}{S_k}$, $\Sigma_B = S_B + \sum_k \frac{g_{Bk}^2}{S_k}$, and $\Gamma = \sum_k \frac{g_{Ak} g_{Bk}}{S_k}$. These results can be derived by direct application of the rule for measuring $\hat{p}$ in the graphical calculus formalism, schematized in Fig. 13.

Employing Eqs. (D1) and (D2) and noticing that $V = 0$, we can reconstruct the covariance matrix of the final pair:

$$\sigma_f = \begin{pmatrix} \frac{\Sigma_B}{\Sigma_A\Sigma_B-\Gamma^2} & -\frac{\Gamma}{\Sigma_A\Sigma_B-\Gamma^2} & 0 & 0 \\ -\frac{\Gamma}{\Sigma_A\Sigma_B-\Gamma^2} & \frac{\Sigma_A}{\Sigma_A\Sigma_B-\Gamma^2} & 0 & 0 \\ 0 & 0 & \Sigma_A & \Gamma \\ 0 & 0 & \Gamma & \Sigma_B \end{pmatrix}. \tag{E2}$$

Notice that this state differs from a graph state by a local phase.

By computing the seralian—defined in Eq. (12)—of the partially transpose covariance matrix of the pair $\tilde{\sigma}_f$ and applying formula (13), we obtain the general lowest symplectic eigenvalue of the partial transpose of the state

$$\nu_-^2 = \frac{(\sqrt{\Sigma_A\Sigma_B} - \Gamma)^2}{\Sigma_A\Sigma_B - \Gamma^2}. \tag{E3}$$

Finally, if we assume that all the modes are equally squeezed in $\hat{p}$ of a factor $R^{-1} = 10^{2s/10}$ and all the CZ-gate correlations have a strength g, we arrive at Eq. (14).

This property of the diamond network, however, is not easily generalized to all graphs that present parallel connections, and the quest for the optimal measurement strategy to improve the final entanglement is by no means trivial. This is the case, for example, of the $\tilde{\mathcal{D}}$ graph shown in Fig. 14, generated by taking the diamond network and adding a CZ-gate link between adjacent central nodes. We can see that for $N > 9$ always measuring $\hat{p}$ in this network is not the optimal strategy, whereas a better strategy is to alternate a $\hat{p}$ and $\hat{q}$ measurement to restore a (smaller) diamond network.

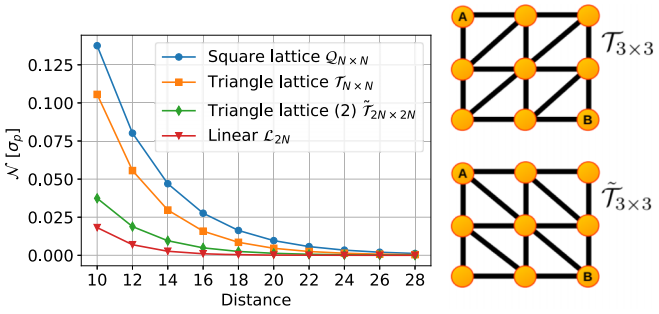

FIG. 18. Comparison between the entanglement capacity between two nodes at the same distance of three lattice graphs, the square lattice $\mathcal{Q}_{N\times N}$ and the two triangles $\mathcal{T}_{N\times N}$, formed from the square by adding edges on the diagonals in such a way that the distance between A and B is the same, $\tilde{\mathcal{T}}_{N\times N}$ formed by adding edges to the diagonals so that the distance is the same as the linear graph, and the linear graph $\mathcal{L}_N$. To compare the networks with the same distance we doubled the size of the $\tilde{\mathcal{T}}$ and the $\mathcal{L}$ graphs.

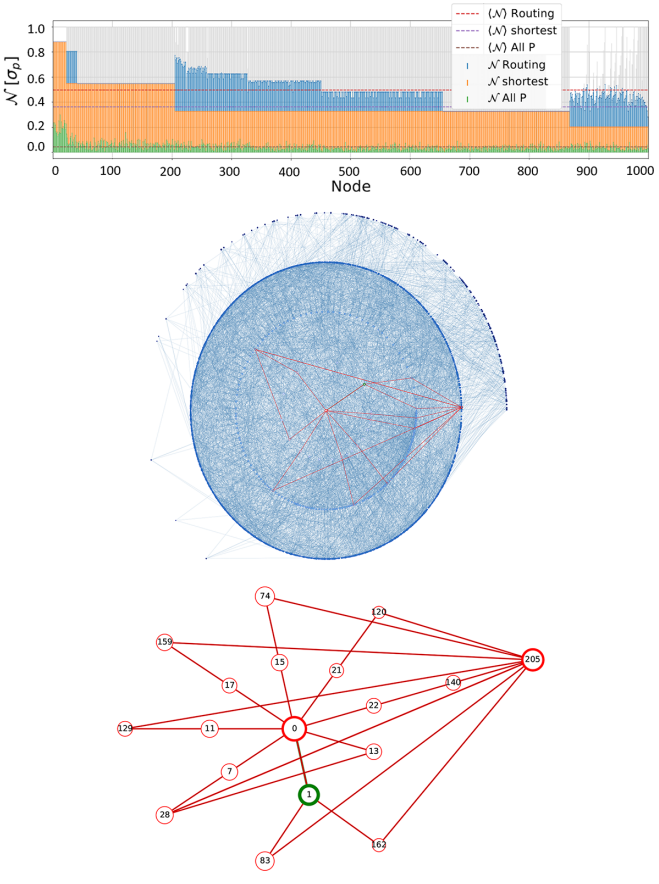

FIG. 19. Negativity produced by the three different protocols applied to each node of the $\mathcal{G}_{ER}(N = 1000, p = 0.4)$ network.

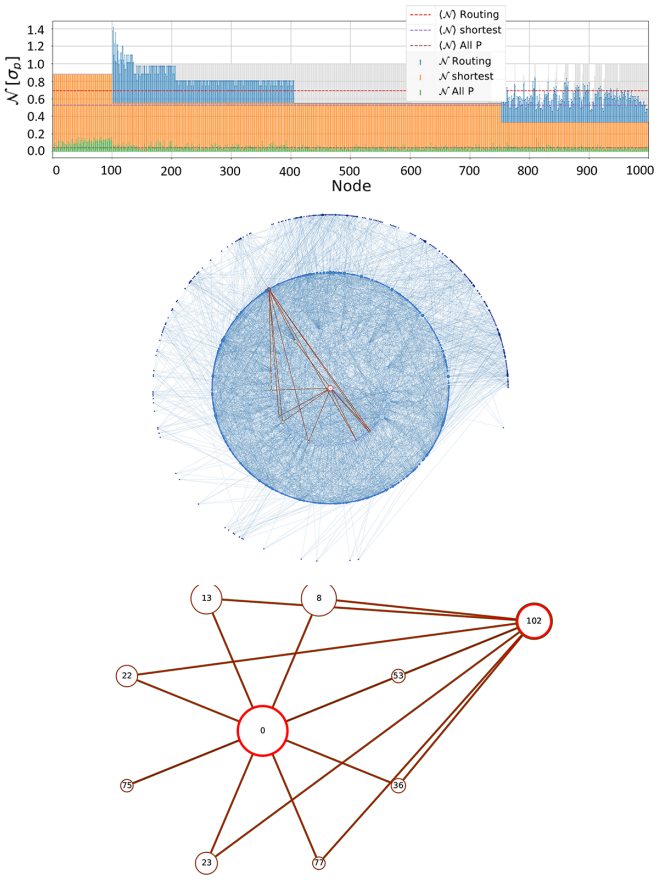

FIG. 20. Negativity produced by the three different protocols applied to each node of the $\mathcal{G}_{BA}(N = 1000, K = 4)$ network.

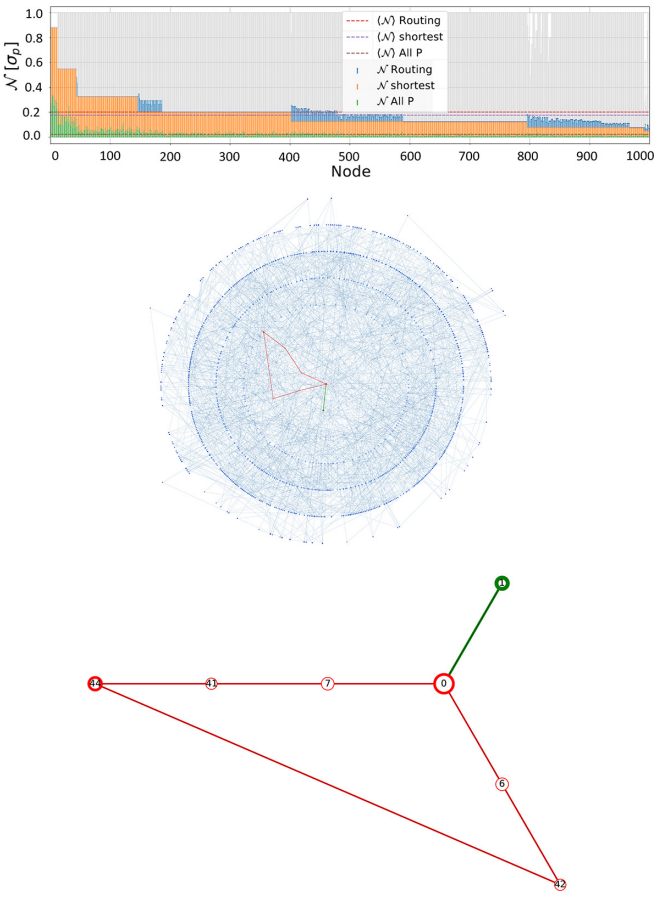

FIG. 21. Negativity produced by the three different protocols applied to each node of the $\mathcal{G}_{WS}(N = 1000, Q = 4, \beta = 0.9)$ network.

Another important figure of merit is the entanglement per squeezing cost, shown in Fig. 15(a).

We see that the diamond is the only one that gives the ratio of entanglement per cost of the network that becomes constant for large N. However, the linear graph is the one that links two nodes that are the farthest away from each other. Conversely, Fig. 15(b) shows the logarithmic negativity in the final pair divided by the number of modes in the initial state. Once again, the diamond structure is particularly convenient, yielding the highest logarithmic negativity while keeping a constant number of independent squeezers.

To give a fair comparison between the capacity of the linear network to bridge distant nodes and that of the diamond to increase the final entanglement we need to generalize the diamond graph to a diamond chain graph, $\mathcal{DC}_{K,N}$, where K is the number of parallel branches linking the two hubs that want to perform quantum communications as in Fig. 16.

We can then compare the entanglement concentrated using multiple path strategies to link two nodes far away from each other. We can see in Fig. 17 that the presence of parallel links has indeed the desired effect, despite the quality of the final pair, which still decreases exponentially with the distance. On the other hand, notice that the parallel links can help concentrate more entanglement until the system reaches a plateau and even the additional channels will not allow one to increase the logarithmic negativity. Moreover, the value for the effort of these networks, specifically the ratio between the entanglement of the pair after the protocol and the squeezing cost before the protocol, is maximized by the linear graph.

Another important class of networks, notably for measurement-based quantum computation, is constituted by grid cluster states that belong to graph shapes that allow for universal quantum computation [41]. Similarly to the diamond network, the presence of ancillary nodes between the emitter and the receiver can improve the quality of the quantum link concerning the linear network. This, however, is not a general rule, and sometimes the presence of additional links can be detrimental. This is the case of the triangular lattice, generated from the square lattice by adding a link between the nodes in the diagonal. There are two ways of generating the triangular, and only one of the two, $\tilde{\mathcal{T}}$, decreases effectively the distance between Alice and Bob. In both cases the result is detrimental; however, $\mathcal{T}$ is slightly better than $\tilde{\mathcal{T}}$, while the square lattice $\mathcal{Q}$ seems to be the most effective. This result is shown in Fig. 18.

APPENDIX F: ROUTING IN COMPLEX NETWORKS

The same analysis of Sec. IV B was done in several networks with different sizes and topologies with very different results that we report in Figs. 19–22. A property that is not apparent in Fig. 9 is that the node with the highest enhancement of entanglement due to the multiple paths is not necessarily

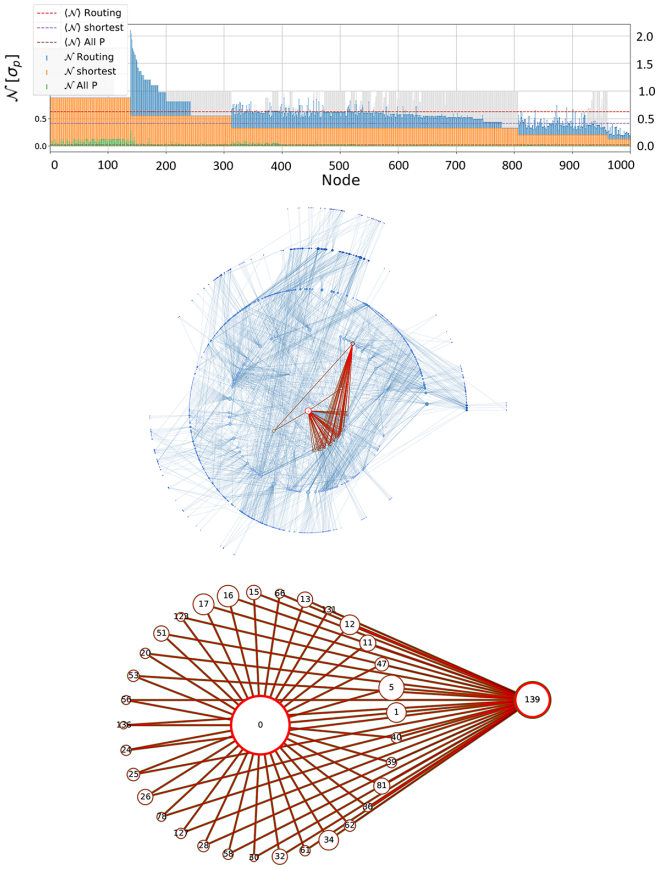

FIG. 22. Negativity produced by the three different protocols applied to each node of the $\mathcal{G}_{WS}(N = 1000, Q = 4, \beta = 0.9)$ network.

the one with the highest logarithmic negativity in absolute. This is the case of the ER network of Fig. 19, in which the node with the highest entanglement, highlighted in green in the graph representation, is at distance 1 while the node with the highest difference in logarithmic negativity between the *Routing* and the *Shortest* protocols, highlighted in red, is at distance 3. In this case, the structure of the subgraph used throughout the *Routing* is not a diamond chain and the intercorrelations among the parallel branches have limited the increase of the entanglement, as for the $\tilde{\mathcal{D}}_N$ network in Fig. 14. In any case, in this network the nodes at greater distances are the ones that are most affected by our protocol, and, although in some cases many parallel paths have been disregarded, as shown by the height of the gray column, all the nodes at distance 4 received a substantial enhancement.

The results of the simulation on the BA topology of Fig. 20 are similar to the AS, although the first only reaches a distance of 3. The nodes with the highest absolute logarithmic negativity and the highest logarithmic negativity difference produced by the *Routing* protocol coincide and are at distance 2 from Alice, whereas this time the subgraph of is a diamond with no interconnections. Also in this case distance 2 is favorable to perform quantum communications.

The WS structure of Fig. 21, on the other hand, is the worst to apply the *Routing protocol*. Only a few nodes were poorly enhanced and mostly at large distances, while the logarithmic negativity averaged over all the nodes for *Routing* and *Shortest* is comparable. Node 44 at distance 3 is the one that received the greatest boost from our protocol, whereas node 1 (like all the other nodes at distance 1) has the highest logarithmic negativity.

Finally, the biological network of Fig. 22 produced the most interesting results. Once again, many nodes at distance 2 end up having more logarithmic negativity than those at distance 1, and at this distance, the nodes with the same degree have the same logarithmic negativity that decreases exponentially with their degree. The nodes with the highest logarithmic negativity and highest difference coincide with node 139, which is linked to Alice through 33 intermediate nodes, forming a diamond network with no interconnections.

[1] S. Wehner, D. Elkouss, and R. Hanson, Quantum internet: A vision for the road ahead, Science **362**, eaam9288 (2018).

[2] S. Pirandola, End-to-end capacities of a quantum communication network, Commun. Phys. **2**, 51 (2019).

[3] M. Pant, H. Krovi, D. Towsley, L. Tassiulas, L. Jiang, P. Basu, D. Englund, and S. Guha, Routing entanglement in the quantum internet, npj Quantum Inf. **5**, 25 (2019).

[4] X. Guo, C. R. Breum, J. Borregaard, S. Izumi, M. V. Larsen, T. Gehring, M. Christandl, J. S. Neergaard-Nielsen, and U. L. Andersen, Distributed quantum sensing in a continuous-variable entangled network, Nat. Phys. **16**, 281 (2020).

[5] G. Bianconi, A. Arenas, J. Biamonte, L. D. Carr, B. Kahng, J. Kertesz, J. Kurths, L. Lü, C. Masoller, A. E. Motter *et al.*, Complex systems in the spotlight: Next steps after the 2021 Nobel Prize in physics, J. Phys. Complex. **4**, 010201 (2023).

[6] M. Chen, N. C. Menicucci, and O. Pfister, Experimental realization of multipartite entanglement of 60 modes of a quantum optical frequency comb, Phys. Rev. Lett. **112**, 120505 (2014).

[7] Y. Cai, J. Roslund, G. Ferrini, F. Arzani, X. Xu, C. Fabre, and N. Treps, Multimode entanglement in reconfigurable graph states using optical frequency combs, Nat. Commun. **8**, 1 (2017).

[8] S. Yokoyama, R. Ukai, S. C. Armstrong, C. Sornphiphatphong, T. Kaji, S. Suzuki, J.-i. Yoshikawa, H. Yonezawa, N. C. Menicucci, and A. Furusawa, Ultra-large-scale continuous-variable cluster states multiplexed in the time domain, Nat. Photonics **7**, 982 (2013).

[9] W. Asavanant, Y. Shiozawa, S. Yokoyama, B. Charoensombutamon, H. Emura, R. N. Alexander, S. Takeda, J.-i. Yoshikawa, N. C. Menicucci, H. Yonezawa *et al.*, Generation of time-domain-multiplexed two-dimensional cluster state, Science **366**, 373 (2019).

[10] M. V. Larsen, X. Guo, C. R. Breum, J. S. Neergaard-Nielsen, and U. L. Andersen, Deterministic generation of a two-dimensional cluster state, Science **366**, 369 (2019).

[11] J. Nokkala, F. Arzani, F. Galve, R. Zambrini, S. Maniscalco, J. Piilo, N. Treps, and V. Parigi, Reconfigurable optical implementation of quantum complex networks, New J. Phys. **20**, 053024 (2018).

[12] P. Renault, J. Nokkala, G. Roeland, N. Joly, R. Zambrini, S. Maniscalco, P. Jyrki, N. Treps, and V. Parigi, Experimental optical simulator of reconfigurable and complex quantum environment, arXiv:2302.12674.

[13] T. Kouadou, F. Sansavini, M. Ansquer, J. Henaff, N. Treps, and V. Parigi, Spectrally shaped and pulse-by-pulse multiplexed multimode squeezed states of light, APL Photonics **8**, 086113 (2023).

[14] L. S. Madsen, F. Laudenbach, M. F. Askarani, F. Rortais, T. Vincent, J. F. Bulmer, F. M. Miatto, L. Neuhaus, L. G. Helt, M. J. Collins *et al.*, Quantum computational advantage with a programmable photonic processor, Nature (London) **606**, 75 (2022).

[15] I. Suleiman, J. A. H. Nielsen, X. Guo, N. Jain, J. Neergaard-Nielsen, T. Gehring, and U. L. Andersen, 40 km fiber transmission of squeezed light measured with a real local oscillator, Quantum Sci. Tech. **7**, 045003 (2022).

[16] I. J. Tillman, A. Rubenok, S. Guha, and K. P. Seshadreesan, Supporting multiple entanglement flows through a continuous-variable quantum repeater, Phys. Rev. A **106**, 062611 (2022).

[17] J. Eisert, Entanglement in quantum information theory, Ph.D. thesis, University of Potsdam, 2001.

[18] G. Vidal and R. F. Werner, Computable measure of entanglement, Phys. Rev. A **65**, 032314 (2002).

[19] M. B. Plenio, Logarithmic negativity: A full entanglement monotone that is not convex, Phys. Rev. Lett. **95**, 090503 (2005).

[20] J. Roslund, R. M. De Araujo, S. Jiang, C. Fabre, and N. Treps, Wavelength-multiplexed quantum networks with ultrafast frequency combs, Nat. Photon. **8**, 109 (2014).

[21] H. Yonezawa, T. Aoki, and A. Furusawa, Demonstration of a quantum teleportation network for continuous variables, Nature (London) **431**, 430 (2004).

[22] C. Fabre and N. Treps, Modes and states in quantum optics, Rev. Mod. Phys. **92**, 035005 (2020).

[23] V. Roman-Rodriguez, B. Brecht, K. Srinivasan, C. Silberhorn, N. Treps, E. Diamanti, and V. Parigi, Continuous variable multimode quantum states via symmetric group velocity matching, New J. Phys. **23**, 043012, 043012 (2021).

[24] A. Christ, C. Lupo, M. Reichelt, T. Meier, and C. Silberhorn, Theory of filtered type-II parametric down-conversion in the continuous-variable domain: Quantifying the impacts of filtering, Phys. Rev. A **90**, 023823 (2014).

[25] F. Arzani, C. Fabre, and N. Treps, Versatile engineering of multimode squeezed states by optimizing the pump spectral profile in spontaneous parametric down-conversion, Phys. Rev. A **97**, 033808 (2018).

[26] E. Gouzien, S. Tanzilli, V. D'Auria, and G. Patera, Morphing supermodes: A full characterization for enabling multimode quantum optics, Phys. Rev. Lett. **125**, 103601 (2020).

[27] M. Yukawa, R. Ukai, P. van Loock, and A. Furusawa, Experimental generation of four-mode continuous-variable cluster states, Phys. Rev. A **78**, 012301 (2008).

[28] D. Barral, M. Walschaers, K. Bencheikh, V. Parigi, J. A. Levenson, N. Treps, and N. Belabas, Versatile photonic entanglement synthesizer in the spatial domain, Phys. Rev. Appl. **14**, 044025 (2020).

[29] J. Arrazola, V. Bergholm, K. Brádler, T. Bromley, M. Collins, I. Dhand, A. Fumagalli, T. Gerrits, A. Goussev, L. Helt *et al.*, Quantum circuits with many photons on a programmable nanophotonic chip, Nature (London) **591**, 54 (2021).

[30] N. C. Menicucci, P. van Loock, M. Gu, C. Weedbrook, T. C. Ralph, and M. A. Nielsen, Universal quantum computation with continuous-variable cluster states, Phys. Rev. Lett. **97**, 110501 (2006).

[31] N. C. Menicucci, S. T. Flammia, and P. van Loock, Graphical calculus for Gaussian pure states, Phys. Rev. A **83**, 042335 (2011).

[32] M. Gu, C. Weedbrook, N. C. Menicucci, T. C. Ralph, and P. van Loock, Quantum computing with continuous-variable clusters, Phys. Rev. A **79**, 062318 (2009).

[33] M. Walschaers, N. Treps, S. Bhuvanesh, L. D. Carr, and V. Parigi, Emergent complex quantum networks in continuous-variables non-Gaussian states, arXiv:2012.15608.

[34] F. Arzani, G. Ferrini, F. Grosshans, and D. Markham, Random coding for sharing bosonic quantum secrets, Phys. Rev. A **100**, 022303 (2019).

[35] O. Pinel, J. Fade, D. Braun, P. Jian, N. Treps, and C. Fabre, Ultimate sensitivity of precision measurements with intense gaussian quantum light: A multimodal approach, Phys. Rev. A **85**, 010101(R) (2012).

[36] M. Gessner, L. Pezzè, and A. Smerzi, Sensitivity bounds for multiparameter quantum metrology, Phys. Rev. Lett. **121**, 130503 (2018).

[37] L. Lami, B. Regula, X. Wang, R. Nichols, A. Winter, and G. Adesso, Gaussian quantum resource theories, Phys. Rev. A **98**, 022335 (2018).

[38] M. Idel, D. Lercher, and M. M. Wolf, An operational measure for squeezing, J. Phys. A: Math. Theor. **49**, 445304 (2016).

[39] A. E. Brouwer and W. H. Haemers, *Spectra of Graphs* (Springer Science & Business Media, Eindhoven, 2011).

[40] D. Cvetkovic, M. Doob, and H. Sachs, *Spectra of Graphs: Theory and Applications* (Wiley, Eindhoven, 1999).

[41] M. Van den Nest, A. Miyake, W. Dür, and H. J. Briegel, Universal resources for measurement-based quantum computation, Phys. Rev. Lett. **97**, 150504 (2006).

[42] M. E. J. Newman, *Networks*, 2nd ed. (Oxford University Press, Oxford, 2018).

[43] A. L. Barabási, *Networks Science* (Cambridge University Press, Cambridge, 2016).

[44] P. Erdős and A. Rényi, On the evolution of random graphs, Publ. Math. Inst. Hung. Acad. Sci **5**, 17 (1960).

[45] M. E. Newman, The structure and function of complex networks, SIAM Rev. **45**, 167 (2003).

[46] A. Elmokashfi, A. Kvalbein, and C. Dovrolis, On the scalability of BGP: The roles of topology growth and update rate-limiting, in *Proceedings of the 2008 ACM CoNEXT Conference* (Association for Computing Machinery, New York, 2008), pp. 1–12.

[47] I. Ispolatov, P. L. Krapivsky, and A. Yuryev, Duplication-divergence model of protein interaction network, Phys. Rev. E **71**, 061911 (2005).

[48] F. Mascherpa, A. Smirne, A. D. Somoza, P. Fernández-Acebal, S. Donadi, D. Tamascelli, S. F. Huelga, and M. B. Plenio, Optimized auxiliary oscillators for the simulation of general open quantum systems, Phys. Rev. A **101**, 052108 (2020).

[49] I. J. Farkas, I. Derényi, A.-L. Barabási, and T. Vicsek, Spectra of real-world graphs: Beyond the semicircle law, Phys. Rev. E **64**, 026704 (2001).

[50] E. P. Wigner, On the distribution of the roots of certain symmetric matrices, Ann. Math. **67**, 325 (1958).

[51] P. van Loock and S. L. Braunstein, Multipartite entanglement for continuous variables, Quantum Info. Conti. Variables 111 (2003).

[52] H. Leone, N. R. Miller, D. Singh, N. K. Langford, and P. P. Rohde, QuNet: Cost vector analysis and multi-path entanglement routing in quantum networks, arXiv:2105.00418.

[53] C. Meignant, D. Markham, and F. Grosshans, Distributing graph states over arbitrary quantum networks, Phys. Rev. A **100**, 052333 (2019).

[54] C. Meignant, D. Markham, and F. Grosshans, Classical-quantum network coding: A story about tensor, arXiv:2104.04745.

[55] B. Zhang and Q. Zhuang, Entanglement formation in continuous-variable random quantum networks, npj Quantum Inf. **7**, 33 (2021).

[56] Q. Zhuang and B. Zhang, Quantum communication capacity transition of complex quantum networks, Phys. Rev. A **104**, 022608 (2021).

[57] J. P. Moutinho, A. Melo, B. Coutinho, I. A. Kovács, and Y. Omar, Quantum link prediction in complex networks, Phys. Rev. A **107**, 032605 (2023).

[58] M. Cuquet and J. Calsamiglia, Limited-path-length entanglement percolation in quantum complex networks, Phys. Rev. A **83**, 032319 (2011).

[59] C. Harney and S. Pirandola, Analytical methods for high-rate global quantum networks, PRX Quantum **3**, 010349 (2022).

[60] N. R. Solomons, A. I. Fletcher, D. Aktas, N. Venkatachalam, S. Wengerowsky, M. Lončarić, S. P. Neumann, B. Liu, Ž. Samec, M. Stipčević *et al.*, Scalable authentication and optimal flooding in a quantum network, PRX Quantum **3**, 020311 (2022).

[61] S. K. Joshi, D. Aktas, S. Wengerowsky, M. Lončarić, S. P. Neumann, B. Liu, T. Scheidl, G. C. Lorenzo, Ž. Samec, L. Kling *et al.*, A trusted node–free eight-user metropolitan quantum communication network, Sci. Adv. **6**, eaba0959 (2020).

[62] F. Hahn, A. Pappa, and J. Eisert, Quantum network routing and local complementation, npj Quantum Inf. **5**, 76 (2019).

[63] S. Pirandola and S. Mancini, Quantum teleportation with continuous variables: A survey, Laser Phys. **16**, 1418 (2006).

[64] C. Weedbrook, S. Pirandola, R. García-Patrón, N. J. Cerf, T. C. Ralph, J. H. Shapiro, and S. Lloyd, Gaussian quantum information, Rev. Mod. Phys. **84**, 621 (2012).

[65] R. Simon, Peres-Horodecki separability criterion for continuous variable systems, Phys. Rev. Lett. **84**, 2726 (2000).

[66] M. Ohliger, K. Kieling, and J. Eisert, Limitations of quantum computing with Gaussian cluster states, Phys. Rev. A **82**, 042336 (2010).

[67] N. Acosta-Mendoza, A. Gago-Alonso, and J. E. Medina-Pagola, Frequent approximate subgraphs as features for graph-based image classification, Knowledge-Based Systems **27**, 381 (2012).

[68] O. Jones, Spectra of simple graphs, Whitman College, Walla-Walla, WA (2013).